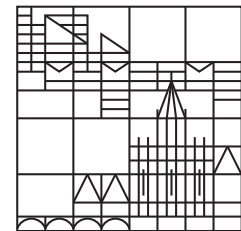
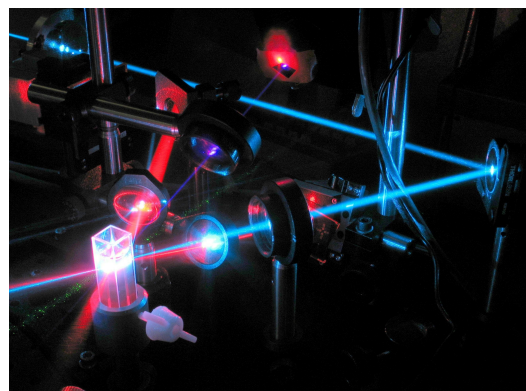


UNIVERSITÄT KONSTANZ
FACHBEREICH PHYSIK

LEHRSTUHL
PROF. DR. P. LEIDERER



Laserinduced nanobubbles



Diploma thesis

presented by
Stefan Weber

Konstanz, 18th of June 2007

Erstgutachter: Prof. Dr. Johannes Boneberg
Zweitgutachter: Prof. Dr. Thomas Dekorsy

Title: Setup for the time resolved extinction measurements at four wavelengths.

Zusammenfassung

Erstmals wurde an diesem Lehrstuhl das Blasenwachstum an nanoskopischen Grenzflächen, genauer gesagt an den Oberflächen von Gold-Nanopartikeln in Wasser, untersucht. Deren plasmonische Eigenschaften stellten sich als ein sehr empfindlicher Indikator für Veränderungen in den dielektrischen Eigenschaften in und um das Partikel heraus. Durch die gleichzeitige Messung bei vier verschiedenen Wellenlängen konnte der Einfluss einer thermischen Anregung durch einen Laserpuls auf die optischen Eigenschaften sowohl nahe der Plasmonresonanz (488 nm, 561 nm¹ und 635 nm), als auch im Bereich der Interband-Absorption (405 nm) und der langwelligen Flanke der Plasmonresonanz (660 nm) untersucht werden. Durch den Vergleich von zeitaufgelösten Extinktionsmessungen mit 50 nm und 80 nm Goldpartikel-Suspensionen mit Mie-Simulationen, die die makroskopischen, temperaturabhängigen dielektrischen Funktionen der beteiligten Materialien enthielten, konnte der Mechanismus für das Blasenwachstum um die Partikel abgeleitet werden.

Schon bei niedrigen Pulsenergien konnten Veränderungen in der Absorption der Proben durch das Aufheizen von Partikel und Umgebung festgestellt werden (“*low fluence regime*”). Das Ausbilden einer Dampfschicht an der Oberfläche des Partikels bei höheren eingestrahlten Fluorzen führt zum Entkoppeln der plasmonischen Oszillationen vom umgebenden Dielektrikum, dem Wasser (“*medium fluence regime*”). Dies führt zu einem Abfall der Extinktion im sichtbaren Spektralbereich. Die Bildung einer Blase kann besonders gut im Signal des Abfragelasers bei 488 nm beobachtet werden, da hier der Effekt des Aufheizens von Partikel und Umgebung (ein Anstieg der Extinktion) genau entgegengesetzt zu dem Effekt der Blasenbildung ist. Mit steigender Fluorze des anregenden Lasers werden auch die Blasen immer größer und schließlich dominiert das Streuvermögen der Blasen die optischen Eigenschaften der Probe (“*high fluence regime*”). Die Extinktion zeigt das Verhalten, das man von Dampfbläschen in Wasser erwarten würde: die kurzen Abfrage-Wellenlängen werden stärker gestreut als die langen. Schließlich wird die Probe für einige nanosekunden vollständig undurchsichtig, sie zeigt ein “Optical Limiting”-Verhalten.

In einem weiteren Experiment wurde gezeigt, dass die Empfindlichkeit des Aufbaus durch die Verwendung von Abfrage-Wellenlängen nahe der Plasmon-Resonanz noch weiter gesteigert werden kann. Des Weiteren wurde die Wellenlänge des Pulslasers

¹Der Laser bei 561 nm kam nur für eine letzte Messung zum Einsatz (vgl. Abschn. 4.5).

in den ultravioletten Bereich verlegt, da die Absorption hier weniger empfindlich auf Veränderungen im Partikel und seiner Umgebung reagiert. Die Wesentlichen Merkmale der vorherigen Messungen konnten reproduziert werden. Außerdem bestätigte sich die Vorhersage der Mie-Theorie, dass im grünen und gelben Spektralbereich erheblich stärkere Signale zu erwarten sind.

Contents

1	Introduction	1
2	Basic theory and state of research	3
2.1	Optical properties of metal nanoparticles	3
2.1.1	The quasistatic approximation	3
2.1.2	Mie theory	5
2.2	Laser induced heating of gold nanoparticles	6
2.2.1	The first picoseconds of a plasmon	7
2.2.2	Heat conduction in and around the particle	8
2.2.3	Superheating and bubble nucleation	10
2.3	Previous publications	11
3	Experimental setup	15
4	Results and discussion	19
4.1	Optical extinction spectra	21
4.2	The low fluence regime	22
4.2.1	Results	22
4.2.2	Discussion	23
4.3	The medium fluence regime	25
4.3.1	Results	25
4.3.2	Discussion	26
4.4	The high fluence regime	28
4.4.1	Results	28
4.4.2	Discussion	30
4.5	Experiments with uv-excitation and a yellow probe laser	32
5	Outlook	35
Summary		36
A	Mie theory	39
B	Temperature dependent optical constants of gold	43

Contents

C One dimensional heat transfer	47
Bibliography	49

1 Introduction

Nanosscopic matter sometimes acts completely different from bulk material. This effect is very pronounced for metal nanoparticles. Bulk gold, for example, is yellow and shiny, whereas gold nanoparticles suspended in water show colours from dark red to pale orange, depending on size distribution and concentration. One of the first applications for these particles was in fact to give glass (e.g. in church windows) an intense red colour. Even from Roman times the use of metal nanoparticle doped glasses was reported (see Fig. 1.1). These unique optical properties originate from collective oscillations in the electron gas of the particle, that lead to a highly increased light scattering and absorption. In the case of gold nanoparticles with diameters below 100 nm the absorption peak is in the green spectral range; hence the intense red colour.

What does this have to do with nanobubbles? Thanks to their absorption properties, metal nanoparticles can reach very high temperatures in a very short span of time by pulsed laser irradiation. The subsequent heat dissipation can lead to a phase transition in the surrounding matrix (e.g. water). This effect can be utilized for numerous applications:

- Functionalized metal nano- and microparticles, that selectively bind to biological structures such as tumours and other diseased cells or bacteria, can

Figure 1.1: The Lycurgus Cup is a richly decorated beaker that dates back to Roman times (fourth century AD). It depicts King Lycurgus of Thrace being dragged to the underworld. The glass appears green in daylight (reflected light) and red when light is transmitted from the inside of the vessel. These unique properties can be ascribed to scrap metal (gold in this case, see [Wag00]), that the Roman craftsmen habitually worked into the glass in order to colour it.



act as localized microabsorbers. The illumination with intense pulsed laser radiation leads to the creation of high peak temperatures that destroy the targeted structures [Pit03, Lap06]. By using laser wavelengths that are strongly absorbed by the particles and not by the surrounding tissue, a highly localized energy deposition can be accomplished. The explosive formation of vapour bubbles around the nanoparticles then leads to the mechanical destruction of cellular structures [Neu03, Neu05, Zha05].

- The scattering behaviour of the vapour bubbles can be used for the design of nonlinear optical devices. There has been an increased interest in effect of Optical Limiting, i.e. on materials that remain transparent at low to moderate fluences and become opaque at a certain threshold fluence. In gold nanoparticle suspensions, the formation of vapour bubbles following laser irradiation can lead to an increased scattering and finally the transmission is thoroughly suppressed [Fra00, Fra01].
- Rapid phase transitions following localized laser induced heating is a crucial issue for Steam Laser Cleaning. The efficient removal of microscopic contaminations on sensitive surfaces, such as semiconductor or data storage devices, has become more and more important, as structures become smaller and smaller. For Steam Laser Cleaning a thin liquid film is condensed onto the substrate and then irradiated with a short laser pulse. The energy absorption in the substrate leads to a fast temperature increase both in the substrate and, due to heat transport, in the liquid film. Bubble nucleation at the solid-liquid interface and the subsequent explosive vaporization of the liquid cause the removal of contaminants [Ime91, Zap91, Mos00]. This process can be seen as the “one dimensional version” of the Optical Limiting mechanism.

A number of previous works on Steam Laser Cleaning [Yav97, Mos00, Dob01, Lan02] and liquid-vapour phase transitions on planar surfaces [Yav94, Lan04, Lan06] gave the motivation for this work. For the interpretation of these studies, an ideally flat surface was assumed. The impact of surface roughness or contaminations as nucleation centres for the bubble formation has not been clarified satisfactorily, so far. The aim of the present work is to study the bubble dynamics far away from a surface on defined “impurities”, viz. gold nanoparticles.

In the following chapter the basic principles of the optical properties of metal nanoparticles will be introduced. Furthermore, an overview over the basic mechanisms of the heat transfer from the heated particle to the surrounding water layers will be given, followed by a collection of publications related to pulsed laser - nanoparticle interaction. After a brief explanation of the experimental setup in Chapter 3 the results of the experiments and their interpretation will be given in Chapter 4.

2 Basic theory and state of research

2.1 Optical properties of metal nanoparticles

The optical properties of gold nanoparticles in the visual spectral range are dominated by collective excitations of the conduction electrons called *plasmon polaritons* or simply *plasmons*¹. They can be induced by external electromagnetic waves. In the following sections a simple electrostatic model for plasmonic oscillations in metal clusters will be derived and the exact electrodynamic calculation for the Problem, the *Mie-theory*, will be introduced.

2.1.1 The quasistatic approximation

The response of a metal sphere of radius R in an external electric field is well known from standard textbooks [Jac99]. The polarizability α links the polarization \vec{P} of the sphere to the external electric Field \vec{E}_0 by

$$\vec{P} = \alpha \vec{E}_0 \quad \text{with} \quad \alpha = 4\pi\epsilon_0 R^3 \frac{\epsilon - \epsilon_m}{\epsilon + 2\epsilon_m} , \quad (2.1)$$

where ϵ and ϵ_m are the static dielectric constants of the sphere and the surrounding medium, respectively.

This result from classic electrodynamics also applies to a very small metal sphere in an oscillating electromagnetic field (wavelength λ) under certain assumptions:

- $\lambda \gg R$: That implies a constant phase of the external electromagnetic field to any given time over the particle volume. This regime is called the *quasistatic regime*.

¹The term *surface plasmon* is often used in connection with the optical excitation of metal clusters. Surface Plasmons, however, usually have a penetration depth of some ten to twenty nanometres; so in nanoscopic particles most of the electrons will participate in the collective motion of the plasmon.

- Excitations due to the magnetic field of the wave do not occur (i.e. the permeability $\mu = 1$). For the visual spectral range and its high frequencies this is a reasonable assumption.
- Instead of the static dielectric constant ϵ the frequency dependent dielectric functions $\epsilon(\omega)$ of the bulk materials are used.
- The dielectric function ϵ_m of the medium is usually taken as a real constant throughout the visible spectral range.

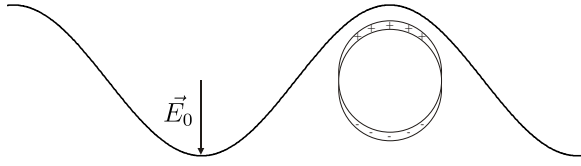


Figure 2.1: Schematic of dipolar plasmon excited by an external electromagnetic wave.

The polarization of the particle shows a resonance behaviour, when the denominator in α (Eq. 2.1) takes its minimum:

$$|\epsilon(\omega) + 2\epsilon_m| = \text{min.}$$

With a complex dielectric function $\epsilon(\omega) = \epsilon_1(\omega) + i \epsilon_2(\omega)$ this can be written as

$$[\epsilon_1(\omega) + 2\epsilon_m(\omega)]^2 + [\epsilon_2(\omega)]^2 = \text{min}, \quad (2.2)$$

Assuming that close to the resonance $\epsilon_2(\omega)$ is small (i.e. small damping) or that its frequency dependence is small ($\partial\epsilon_2/\partial\omega \approx 0$), the resonance condition is given by

$$\epsilon_1(\omega) = -2\epsilon_m. \quad (2.3)$$

For small particles ($R < 10 \text{ nm}$) this gives a good approximation of the resonance position. For larger particles the inner field distribution is no longer homogeneous and has to be developed by multipole expansions. This is done in the Mie theory, which will be introduced in the next section. But also for very small clusters ($R < 1 \text{ nm}$) deviations from the quasistatic approximation arise. In this size range the bulk dielectric functions can no longer be used for several reasons; for example, the mean free path of the electrons is limited by the particle dimensions; furthermore the influence of the surface compared to the volume becomes dominant. However, the gold spheres used in this work are in the size range above 10 nm, so the use of bulk dielectric functions for the calculations is justified. For a more detailed discussion of the intrinsic size effects of the optical properties of metal clusters the reader is referred to Chapter 2.1 in [Kre95].

2.1.2 Mie theory

In the beginning of the 20th century Gustav Mie gave a general solution to the problem of a sphere of arbitrary size and material exposed to an electromagnetic wave [Mie08]. He formulated appropriate boundary conditions and applied the Maxwell equations using spherical coordinates and multipole expansions. Input parameters are the dielectric functions of the sphere and the adjacent medium and - in contrast to the quasistatic theory - the particle radius R . The most striking feature of this work is that it applies for a wide range of different applications. The scattering behaviour of macroscopic objects, such as raindrops under irradiation of radar rays, can be computed as well as the behaviour of microscopic colloidal systems exposed to visible light.

In the context of the Mie theory a set of equations for absorption, scattering and extinction cross sections (σ_{abs} , σ_{sca} and σ_{ext}) can be derived. In this context, cross section means that the intensity loss of a homogeneous parallel beam of light after passing one single nanoparticle equals the intensity loss by an ideally absorbing surface with a surface area of σ . This is either due to dissipative losses (σ_{abs}) or due to elastic scattering (σ_{sca}) with the total loss being $\sigma_{ext} = \sigma_{abs} + \sigma_{sca}$. In a system with a number density $n = N/V$ of particles, the intensity loss $\Delta I(z)$ is given by

$$\Delta I(z) = I_0 \cdot (1 - \exp(-n\sigma_{ext} \cdot z)) \quad (2.4)$$

Such a behaviour is often called a *Lambert-Beer law*. Although the Mie theory gives an exact solution to the problem, its formalism is lengthy and explicit calculations are very time consuming. Nowadays this is mostly done numerically by computer programs. In the present work the freeware program "MiePlot" [Lav06] was used to compute spectral cross sections. The basic ideas of the mathematical formalism are given in Appendix A.

However for the quasistatic regime ($R \ll \lambda$) multipole orders higher than the dipole can be neglected and the Mie formulas are simplified considerably. The extinction cross section is in this case given by:

$$\sigma_{ext}(\omega) = \frac{9\omega}{c} \epsilon_m^{3/2} V_0 \frac{\epsilon_2(\omega)}{[\epsilon_1(\omega) + 2\epsilon_m]^2 + [\epsilon_2(\omega)]^2} \quad (2.5)$$

The maximum of extinction is reached when the denominator takes its minimum. This leads to a resonance condition that is already known from Eq. (2.3): $\epsilon_1(\omega) = -2\epsilon_m$. Furthermore, the influence of the surrounding medium can be studied. If the sphere material acts like a Drude metal with $\epsilon_1 \approx 1 - \frac{\omega_p^2}{\omega^2}$ (i.e. ϵ_1 is monotonically growing with respect to the frequency; ω_p is the plasma frequency), an increasing ϵ_m leads to a redshift of the plasmonic peak extinction.

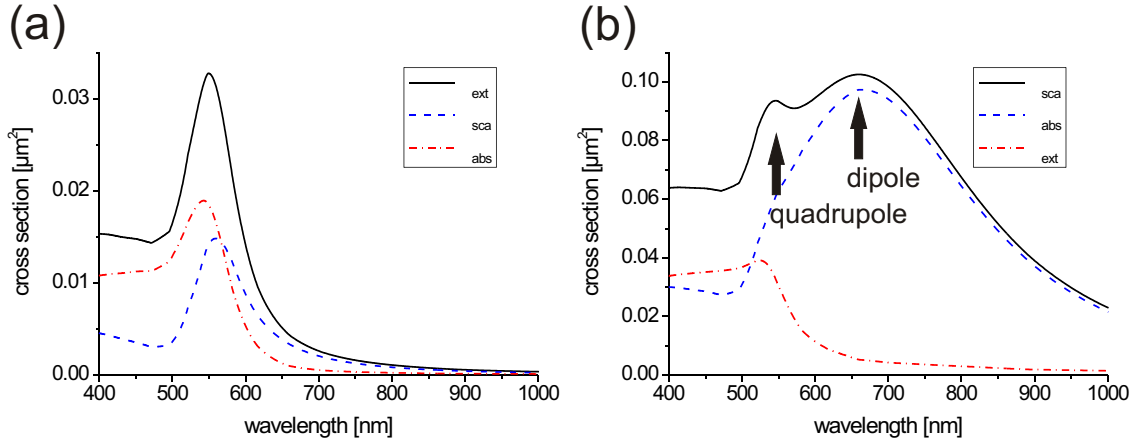


Figure 2.2: Simulated spectral cross sections for gold spheres with (a) 80 nm and (b) 160 nm diameter. For the larger sphere the dipole resonance is shifted to the red and an additional peak associated with the quadrupole resonance appears. Spectra generated with MiePlot [Lav06].

Some results of numerical calculations for gold particles suspended in water are given in Fig. 2.2. The plots show that for smaller particles (80 nm diameter) the dipolar mode is very pronounced. When the particle radius is increased, this mode is broadened and shifted to the red. Additionally, a second peak appears around 550 nm, which can be ascribed to the quadrupole resonance. The extinction plateau on the short wave side of the resonance can be explained by interband transitions from the densely populated d -band to higher conduction bands. The threshold for interband absorption in gold is at a photon energy of 2.4 eV to 2.5 eV (about 510 nm) [Kre95].

2.2 Laser induced heating of gold nanoparticles

In the last chapters the response of metal spheres to light irradiation was discussed, assuming that the absorbed energy does not cause any modifications in the particle or the surrounding water layers. For continuous wave irradiation the generated heat is dissipated fast enough to justify this assumption. Calculations show a temperature increase for a 100 nm diameter gold particle in water being irradiated with a focused 6 W, 532 nm (190 W/mm^2) continuous wave laser of 10 K, which is negligible (see chapter 8.2 in [Dah06]). Pulsed lasers, on the other hand, can easily reach a power of some gigawatts for very short times. The processes coupled with the relaxation of the non-equilibrium state after a laser pulse will be discussed in the following sections.

2.2.1 The first picoseconds of a plasmon

The dynamics in a metal nanoparticle following an ultrashort laserpulse has been studied very detailed in the past decade. In order to separate the different relaxation steps, most studies used pico- or femtosecond laser pulses. With pump-probe experiments the changes in the optical transmission around the plasmon resonance peak were observed with picosecond resolution (see for example [Har04]). From the results of these studies the thermalization mechanism of the laser pulse energy in a metal particle could be inferred. It can be subdivided into three steps:

1. *Excitation of the electron gas*

Usually the absorption of a laser pulse (with frequency ω) in noble metals is due to intraband-absorption². So electrons from the interval $[\epsilon_F - \hbar\omega, \epsilon_F]$ below the fermi energy ϵ_F are excited to an interval $[\epsilon_F, \epsilon_F + \hbar\omega]$ leaving the electron distribution in a non-equilibrium state. Via electron-electron scattering the system reaches a hot fermi distribution. For gold this thermalization process usually takes 500 fs [Fat00].

2. *Energy transfer to the lattice*

During and after the equilibration of the electron gas, energy is being transferred to the lattice by electron - phonon scattering. Typical relaxation times for gold are in the order of 1 ps [Fat01]. For the sake of completeness it should be mentioned that the rapid increase in the lattice temperature and the corresponding expansion can excite vibrational modes in the particle with periods around ten picoseconds and damping times of 100 ps [Har06, Ple07].

3. *Heat transfer to the matrix*

The last step is the dissipation of the thermal energy into the surrounding medium. In nanoscopic metal particles the surface area is found to have a big influence. Typical values for the cooling time τ in aqueous goldparticle suspensions at low excitation powers are found to be in the order of 10 ps to 380 ps for diameters ranging from 5 nm to 50 nm, τ being proportional to R^2 [Hu02].

All these mechanisms are in the sub-nanosecond regime. The excitation in the experiments for the present work had been performed with pulse durations of 10 ns; so the first two steps of thermalization should play no decisive role. Whether the last step might become important will be discussed in the following section, where the relevant heat transfer mechanisms will be addressed in more detail.

²The lifetime of holes in the d -band caused by interband absorption is usually some tens of femtoseconds in noble metals [Mat99]. Most of the recombination energy is transferred to the conduction band electrons, so assuming pure intraband absorption is feasible.

2.2.2 Heat conduction in and around the particle

The basic equation for diffusive heat propagation is given by:

$$\frac{\partial T}{\partial t}(\vec{r}, T) - \kappa \Delta T(\vec{r}, T) = \frac{A(\vec{r}, T)}{\rho c_p}, \quad (2.6)$$

where $A(\vec{r}, T)$ is a heat source, ρc_p is the volumetric heat capacity and κ the diffusion constant or diffusivity of the material (see for example [Car59]). In most publications κ and c_p are assumed to be temperature independent; for the materials used in this work this temperature dependence is in fact not very pronounced (see Appendix A in [Neu05]). A convenient approach towards a solution of the problem is to use the Greenfunction of (2.6); i.e. the solution to the problem of a pointlike heat source with infinitely short heating ($A(\vec{r}, T)/\rho c_p = \delta(\vec{r})\delta(t)$):

$$g(\vec{r}, t) = \frac{1}{8\rho c_p (\pi \kappa t)^{3/2}} \exp\left(-\frac{r^2}{4\kappa t}\right). \quad (2.7)$$

The solution for an arbitrary temporal and spacial heat source $A(\vec{r}, T)$ is then obtained by convoluting it with (2.7).

For a rough estimation of the timescales for the equilibration of temperature differences inside a inhomogeneously heated volume the time constant in the exponential function of (2.7) can be used:

$$\tau_{eq} = \frac{R^2}{4\kappa}. \quad (2.8)$$

For a spherical gold particle ($\kappa_{Au} \approx 1.2 \cdot 10^{-4} \text{ m}^2/\text{s}$) with 40 nm radius the thermalization time is 3 ps. So with the excitation time for the experiments in this work being in the order of nanoseconds, a homogeneous temperature distribution inside the particle can be assumed.

For the energy transfer to the surrounding water during a laser pulse (duration τ_L), the thermal diffusion length can be defined:

$$r_{th} = 2\sqrt{\kappa_W \tau_L}. \quad (2.9)$$

For water ($\kappa_W \approx 10^{-7} \text{ m}^2/\text{s}$) and a pulse duration of 10 ns, a layer of 75 nm radius around the heat source can be heated up until the end of the pulse. Of course, these rough approximations neglect some important aspects of the problem:

- *The particle-fluid interface*

For the heat conduction at an interface between different materials the heat

transmission resistance R_c is important. It can lead to a heat confinement inside the particle, that has to be considered in (2.6). The values for nanoscopic spheres can differ considerably from bulk materials and planar surfaces. Approximate values for the thermal conductance coefficient from a metal nanosphere to water were given in [Wil02] and [Ple04]. They obtained a consistent value of $G = 1/R_c \approx 100 \text{ MW/m}^2\text{K}$.

- *Evaporation of the embedding medium*

The high temperatures in the particle give rise to a rapid heating in the surrounding layers of the matrix. If the timescale is short enough, the liquid phase can be superheated and explosive boiling can occur [Kot06]. The formation of a vapour bubble leads to a further heat confinement, as the thermal conductance of steam is approximately a factor 40 lower than the thermal conductance of liquid water.

- *Melting and evaporation of the particle*

Heating metal nanoparticles by pulsed laser irradiation can easily lead to temperatures of some 1000 K inside the sphere [Pus06]. It has been shown that this can result in melting [Ple04] or even the complete destruction of the particles [Kur98, Lin00]. These phase transitions require additional energy in the form of latent heat.

- *Radiative energy loss (a)*

The energy transfer over the particle boundary does not necessarily have to be due to heat conduction only. Every surface that has a temperature above 0 K is a source of thermal radiation according to the Stefan-Boltzmann law:

$$P_r = \hat{\epsilon} \sigma A T^4, \quad (2.10)$$

where A is the surface area and $\hat{\epsilon}$ the surface emissivity; $\sigma = 5.67 \cdot 10^{-8} \text{ J/m}^2\text{sK}^4$ denotes the Stefan-Boltzmann constant.

- *Radiative energy loss (b)*

Another possible radiative loss mechanism would be *photoluminescence*. It was first discovered by Mooradian in 1968 on smooth gold surfaces [Moo69]. The recombination of excited electrons from the conduction band with holes in the d-band give rise to a broadband light emission of the sample. Mooradian reported a quantum efficiency of $\sim 10^{-10}$ for his experiments. Many groups reported an increased efficiency on rough surfaces or on nanoparticles [Boy86, Bev03, Wil98], which suggests a plasmonic contribution to the effect. The emitted radiation in their experiments is mainly in the red and infrared spectral range. Wilcoxon et. al. found the quantum efficiency for gold nanoclusters particles to be in the order of $10^{-4} - 10^{-5}$. Yet, these efficiencies are much too low to give any significant contribution to the energy loss of the particle.

For a liquid gold surface (emissivity $\hat{\epsilon} \approx 0.3$ [Kri90]) at a temperature of 3000 K the energy flux is $J \approx 1.4 \text{ MW/m}^2$. However, thermal conductance of the metal-water interface is many orders of magnitude larger and even the thermal conductance of a 100 nm steam layer around the particle would be in the order of $J_c \approx K \frac{\Delta T}{\Delta r} \approx 500 \text{ MW/m}^2$ (thermal conductivity of steam $K = 0.016 \text{ W/m} \cdot \text{K}$). Hence, the energy loss caused by radiation can be neglected. Whether the emitted radiation might become important for the optical signals will be discussed in Sec. 4.4.2.

2.2.3 Superheating and bubble nucleation

During the process of laser induced heating of nanoparticles, the surrounding fluid can easily reach temperatures far above the boiling temperature for the ambient pressure. The timescales of heating being very short, the boiling may not start instantaneously. Instead, a metastable phase can form, followed by explosive evaporation of the liquid. The liquid-gas phase transition can be described within the scope of the van der Waals model. A van der Waals isotherm at a temperature T below the critical temperature T_c is shown in Fig. 2.3. On the left hand side of the diagram the substance is a pure liquid, on the right it is a pure gas; between the points A and E vapour and liquid phase coexist. The dashed lines denote the limits of metastable states, where the substance can still exist as pure liquid/vapour. The inner line is called the spinodal; underneath this line (between B and D) the material is intrinsically unstable, as $(\frac{\partial P}{\partial V})_T > 0$. The upper temperature limit for the coexistence of liquid and vapour is the critical temperature T_c . Above T_c the pressure $p(V)$ is found to be monotonically decreasing with respect to V , that is, the substance is in a gaslike state called *supercritical fluid*.

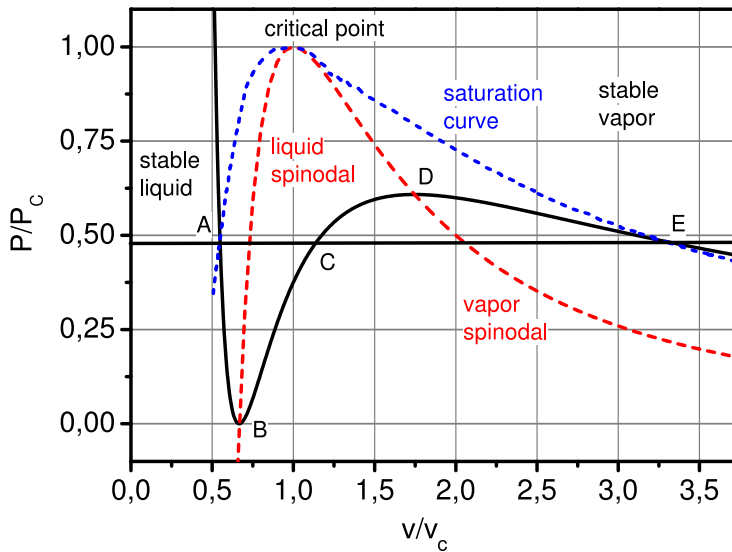


Figure 2.3: P-V diagram for the liquid-vapour transition [Lan06].

Typical values for the lifetime of a superheated liquid in laser-heated systems have been investigated in connection with Steam Laser Cleaning experiments. Lang calculated the temperature behaviour at a planar silicon isopropanol interface upon irradiation with a Nd:YAG pulse [Lan06]. He found that the liquid is in a metastable state for 1.4 ns before bubble nucleation sets in. Of course, these results cannot be transferred directly to the three dimensional situation of a sphere in water. The surface-to-volume fraction is much higher in the three dimensional case and the evaporating liquid has more degrees of freedom for its expansion. Hence, the timescales for the boiling retardation should be smaller. In fact, Plech and coworkers found bubble nucleation by femtosecond excitation to set in after less than 1 ns [Kot06].

2.3 Previous publications

Several groups have been studying the interactions of pulsed lasers with metal nanoparticles in the past decade. Many of them used gold nanoparticles due to their resonance behaviour in the visible spectral range (see section 2.1.2). A beautiful experiment was performed by Hartland and coworkers. They carried out time resolved optical pump probe spectroscopy with a femtosecond Ti:Sapphire system. They used a small fraction of the pump beam and an adjustable delay line to generate a white light continuum probe pulse at a sapphire window. Figure 2.4 shows the result for 40 nm goldspheres in water. Immediately after the laser excitation the extinction around the plasmon resonance (~ 525 nm) is decreasing dramatically, while it increases in the wings of the resonance. The bleaching signal shows a strong drop in the first ten picoseconds followed by a slower decay. The first drop is being ascribed to changes in the occupation of electronic states near the Fermi level following the excitation; the further signal is caused by the slower heat transfer to the environment. The shape of the absorption signals can be described by changes in the dielectric functions due to the excited electrons and the following lattice expansion [Har06].

Optical spectroscopy is a very powerful tool for studying electronic properties of the materials involved. However, structural changes or phase transitions are difficult to probe. Plech and coworkers focussed on time resolved x-ray scattering experiments with gold nanoparticle suspensions after femtosecond excitation. The heating and melting of the particles could be observed [Ple04] as well as the bubble formation around the spheres [Kot06]. For gold particles (diameter 35 nm) they found a maximum bubble lifetime of 2 ns at a fluence of 2000 J/m^2 and estimated a maximum bubble volume of 140 times the particle volume. Additionally, threshold fluences for the respective processes were ascertained by varying the excitation power.

For time resolved experiments pump-probe setups are very useful. However, it is very laborious to get a sufficiently high temporal resolution over a longer span of time,

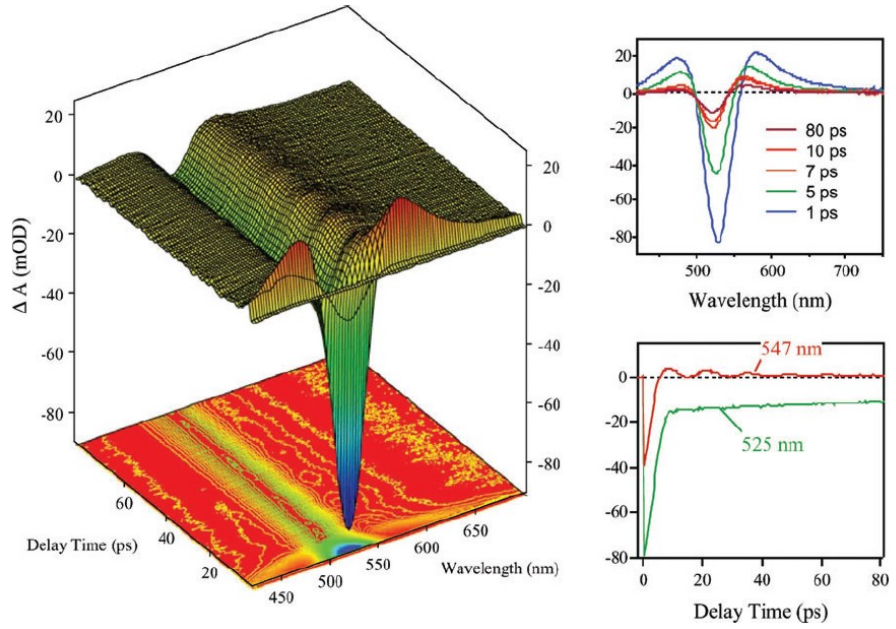


Figure 2.4: Time and wavelength resolved transient absorption change for gold particles of ~ 40 nm diameter suspended in water. Top right: cross sections at different delay times; lower right: temporal evolution of the signal at two wavelengths. The vibration of the particle following the rapid heating of the particle can clearly be seen as oscillation at 547 nm [Har04].

as for every time step an individual measurement has to be performed. Another approach would be to probe the transmission continuously at single wavelengths. Thus, the temporal evolution of the signals can be studied even for very long delay times. Inasawa and coworkers recorded the transmission signals for a 488 nm argon-ion laser and a 635 nm diode laser after irradiating 36 nm diameter gold particles with a 30 ps third harmonic Nd:YAG laser pulse [Ina06]. They found short term absorption changes on a timescale shorter than 50 ns on both wavelengths and permanent changes on the red signal on a timescale of microseconds, which they explain by melting and evaporation of particles. TEM studies show that in addition to the primary particles small clusters of some nanometres had appeared.

The mechanisms of size reduction and shape changes of metal nanoparticles due to pulsed laser irradiation have also been studied. Kurita and coworkers observed the destruction of gold particles by a second harmonic Nd:YAG at a repetition rate of 10 Hz after several minutes. Size reductions of some ten nanometres were reported [Kur98].

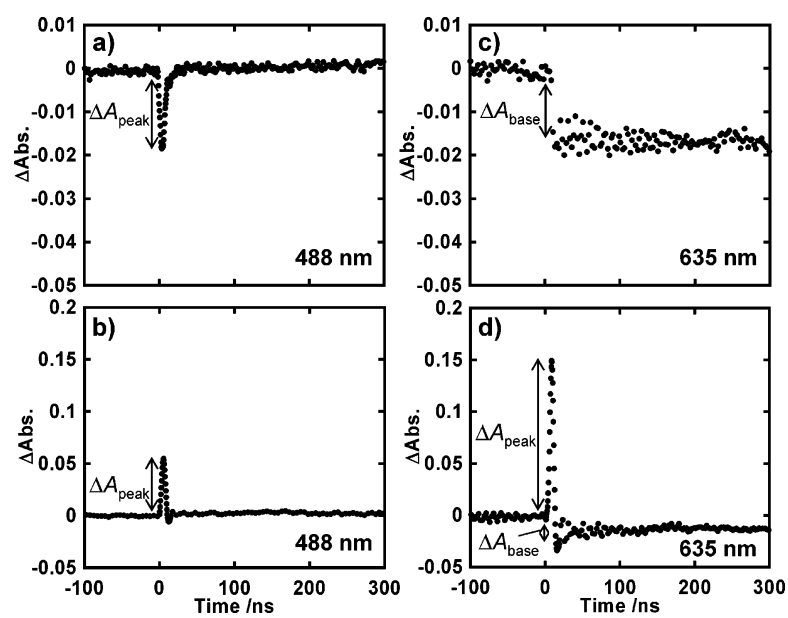


Figure 2.5: Typical transient absorption data from [Ina06]. (a) and (c) were recorded at a laser fluence of 15 mJ/cm^2 and (b) and (d) at 24 mJ/cm^2 .

3 Experimental setup

For the experiments, gold colloid suspensions from British Biocell International (BBI) with particle diameters of 50 nm and 80 nm¹ were used. Goldparticles in this size range were chosen due to their optical properties in the visible spectral range (see chapter 2.1.2), viz. the dipolar resonance in the range around 540 nm. Before and after every experiment optical extinction spectra were recorded with a spectrometer (IKS Optoelectronic/Polytec X-dap).

For the optical measurements glass cells made of special optical glass (Hellma) were used. The light path inside the cells was 2 to 10 mm. Initial studies have been performed with the larger cuvettes. Thanks to the increased probe volume, stronger signals are obtained. On the other hand the filled cuvettes have absorption rates of up to 95%. Thus, the Nd:YAG intensity on the back of the cell is much lower than at the front. Consequently, the probe signals only provide an integral signal for the different laser fluences in the probe volume. To avoid intensity gradients either the particle suspensions can be diluted or the optical path length can be decreased. The advantage of the second option is, that due to the reduced probe volume lateral intensity gradients caused by the gaussian beam profile of the Nd:YAG beam can be diminished.

The setup for the time resolved absorption measurements is shown in Fig. 3.1. The pulselaser source was a Q-switched, seeded Nd:YAG system (Continuum Powerlite), that can be operated with a second and a third harmonic generator, the output wavelength being 532 nm (green) and 355 nm (ultraviolet), respectively. The temporal pulse form can be approximated by a gaussian with a pulse duration of 10 ns FWHM. The pulse energy was controlled by shifting the time between the ignition of the flash lamp and the activation of the Q-switch (Q-swich delay time). A drawback of this method is an increase of the pulse duration towards low energies (either too low or to high Q-switch delay times) of some nanoseconds.

Most experiments were performed with the second harmonic Nd:YAG. The advantage of the green laser pulses is the increased absorption of the gold spheres due to the proximity to the plasmon resonance. However, further analysis showed that the exact position and the shape of the resonance peak is very sensitive to temperature

¹The manufacturer specifies the deviations from the mean diameter to be less than 8% and the particles to be more than 95% spherical.

3 Experimental setup

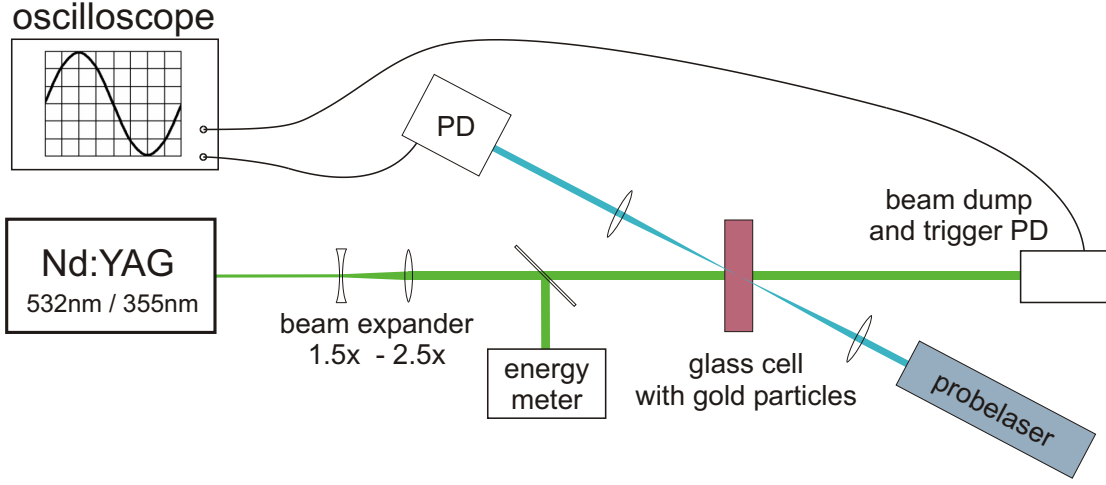


Figure 3.1: Setup of the time resolved absorption measurement. The Nd:YAG beam is expanded, ensuring a homogeneous illumination in the probe volume. A small fraction of the beam is deflected by a glass slide in order to determine the energy of the pulse with an energy meter. Changes in the intensity of the probe beams (only one depicted here) are monitored by a photodiode (PD) and an oscilloscope.

changes both in the particle and in the surrounding water layers. Hence, the absorption coefficient may change during the laser pulse. In the ultraviolet spectral range the absorption is dominated by interband transitions and hence less affected by the temperature of the system. The disadvantages of the ultraviolet beam are a lower conversion efficiency in the third harmonic generator and a decreased stability of the pulse energy.

In order to assure a homogeneous illumination of the particles the beam is expanded by a confocal combination of a biconcave ($f_1 = -100$ mm) and a biconvex ($f_2 = 150$ mm) lens. This configuration with a beam expansion factor of 1.5 has proved to be a good compromise, providing a constant intensity over the whole probe volume at sufficiently high fluences.

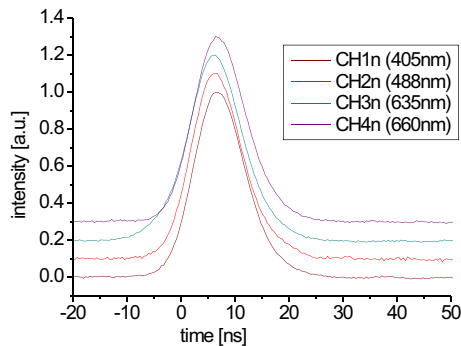


Figure 3.2: Synchronization of the signals. The position of the Nd:YAG pulse was recorded simultaneously with all four photodiodes; deviations of the peak position are below 1 ns.

The extinction of the gold suspensions was probed at four wavelengths simultaneously. On the shortwave side of the plasmon resonance (cp. Fig. 2.2 on page 6) a 405 nm diode laser (Oxxius Violet) was used to probe the response in the interband absorption regime. In the the spectral vicinity of the plasmon peak, an argon-ion laser (Coherent Innova 90) at 488 nm and a diode laser at 635 nm were used. Finally, an additional diode laser at 660 nm was used to probe the red spectral range in the shoulder of the plasmon peak. In a last experiment the 660 nm laser was replaced with a 561 nm continuous wave Nd:YAG², whose wavelength is very close to the plasmon resonance of the 80 nm particles.

All four beams were focussed on the same point in the cell and transmission changes were monitored by photodiodes (FND-100Q, rise time ≈ 1 ns) and by a fast oscilloscope (Tektronix TDS684B, 1GHz 5GS/s). In order to ensure a linear response of the photodiodes, the probe lasers intensities were equalized to a static photodiode signal of 50 – 60 mV. For the data analysis, an exact synchronisation of the signals is vital, as deviations in the lightpath of 10 cm already give rise to a signal shift of 1 ns. Therefore the same lightpaths and cablelengths were chosen for all wavelengths (Fig. 3.2). The Nd:YAG pulses were eliminated from the signals by appropriate edge and interference filters. Thanks to the relatively big sensitive area of the photodiodes (5.1 mm^2) signal changes due to thermal modifications of the refractive indices during the Nd:YAG pulse can be avoided. In order to decrease the effects of the noise from the lasers and the photodiodes the signals were averaged over 20-50 excitation pulses. During the measurement the Nd:YAG-pulse energies were sufficiently stable. In between the pulses there was enough time for the excess heat to diffuse from the probe volume. At higher excitation fluences the cell was stirred after every pulse in order to increase heat diffusion and to replace damaged particles.

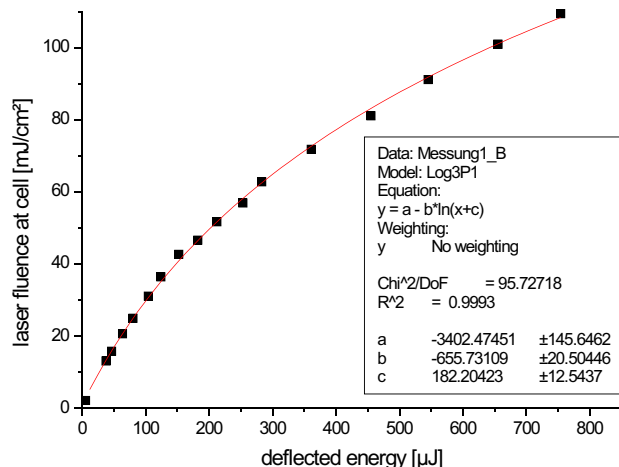


Figure 3.3: Energy calibration graph for 532 nm. The laser fluence at the probe volume can be approximated by a logarithmic fit function (straight line).

²The Nd:YAG laser is operated at the 1122 nm line and intra-cavity frequency doubled. A test laser was kindly provided by Coherent Germany

3 Experimental setup

A very important part of the experiments is the energy calibration of the excitation laser. In order to determine the laser flux at the probe volume a copper plate with a pinhole was placed at the focus of the probe beams. Both the transmitted energy behind the pinhole and the reflection of a glass slide placed in the Nd:YAG beam before the cell (see Fig. 3.1) were recorded with two energy meters (Coherent Field-Master GS with a Pulsehead LM-P2). The energy calibration curve for the 532 nm laser is shown in Fig. 3.3.

4 Results and discussion

For the further interpretation it is vital to define some quantities related to the data recorded in the experiments. The photodiodes are being operated in the linear response regime. Hence, the signals are proportional to the power of the incident radiation I . The *transmittance* T of an object is defined by

$$T = \frac{I}{I_0}, \quad (4.1)$$

I and I_0 being the transmitted and the initial power, respectively. So the signals from the photodiodes are a direct measure for changes in the transmittance of the sample. The *absorbance* is given by

$$A = -\log_{10}(T) = \log_{10}\left(\frac{I_0}{I}\right). \quad (4.2)$$

It depends on the substance and the layer thickness. As a geometry independent measure of the absorption properties of a substance, the *optical density* is defined by normalizing the absorbance by the length l of the light path through the sample:

$$OD = \frac{A}{l} = \frac{1}{l} \log_{10}\left(\frac{I_0}{I}\right). \quad (4.3)$$

If the sample has an extinction behaviour following a Lambert-Beer law (see formula 2.4 on page 5), the transmittance of a layer with optical path length l can be written as

$$\begin{aligned} T(l) &= \frac{I}{I_0} = \exp(-\sigma n \cdot l) \\ \Rightarrow -\ln \frac{I}{I_0} &= \alpha A(l) = \sigma n \cdot l, \end{aligned} \quad (4.4)$$

where σ is the extinction cross section and n the number density of particles; $\alpha = \ln 10 \approx 2.3$ is the correction factor for the decadic logarithm¹.

¹The decadic logarithm is conventional way to express A and OD in spectroscopy. However, the quantitative description requires the natural logarithm.

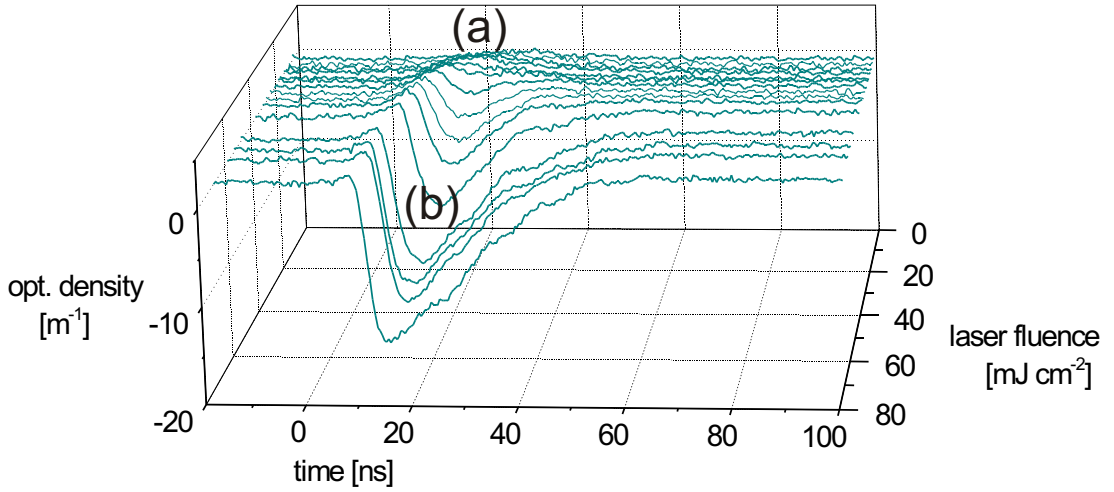


Figure 4.1: Overview over the energy dependence of the extinction signals for a 80 nm goldparticle suspension at 488 nm. A small increase in optical density (a), visible at low excitation fluences (low fluence regime), is being superimposed by a strong drop (b) at higher fluences (medium fluence regime). The high fluence regime could not be assessed in this measurement (see Sec. 4.4).

Hence:

$$\Rightarrow OD \propto \sigma \cdot n, \quad (4.5)$$

Changes in the optical density are directly proportional to changes in the extinction cross section, assuming that the particle concentration remains constant.

It should be stressed at this point that these quantities do not include any information about the loss mechanism. The losses in the transmitted beam can be caused by absorption processes as well as by scattering. So an increase in the optical density of the sample does not necessarily imply that more heat is being generated inside the sample. Therefore, the term *extinction* will be used to describe changes in the transmitted intensity of the probe beams (see also Sec. 2.1.2).

For a better understanding of the optical density changes described in the subsequent sections, the static extinction spectra will be discussed in the next section. It turned out that the optical response of the samples showed distinctive features at different excitation fluences as it can be seen in Fig. 4.1. At a probe wavelength of 488 nm the optical density in the 80 nm goldparticle suspension showed a small increase at low excitation fluences (low fluence regime), followed by a strong drop at higher fluences (medium fluence regime). Hence, the description of the signals will be divided into the low, medium and a high fluence regime. All experiments described in the following three sections have been performed with a excitation wavelength of 532 nm. Every

section will contain a presentation of the results and will be followed by a discussion and interpretation of the signals. Finally, first results of experiments with a yellow probe laser (561 nm) and ultraviolet excitation (355 nm) will be presented.

4.1 Optical extinction spectra

Before and after every experiment optical extinction spectra of the samples were recorded in order to search for irreversible effects caused by the laser irradiation. Plots for fresh particles and a comparison with the predicted extinction from the Mie theory are presented in Fig. 4.2. Using the particle density as a fit parameter, the theoretical curves have been fitted to the same peak height.

The values for the density are in good agreement with the datasheet from the manufacturer: For the 50 nm particles $5.9 \cdot 10^{10} \text{ ml}^{-1}$ are obtained (BBI: $4.5 \cdot 10^{10} \text{ ml}^{-1}$) and for the 80 nm particles $1.0 \cdot 10^{10} \text{ ml}^{-1}$ (BBI: $1.1 \cdot 10^{10} \text{ ml}^{-1}$). The corresponding mean distances between neighbouring particles are 2.6 μm (50 nm) and 4.6 μm (80 nm).

In Table 4.1 the optical density values for the probelaser wavelengths are given together with the corresponding transmission of the 2 mm layer of particle suspension in the glass cells.

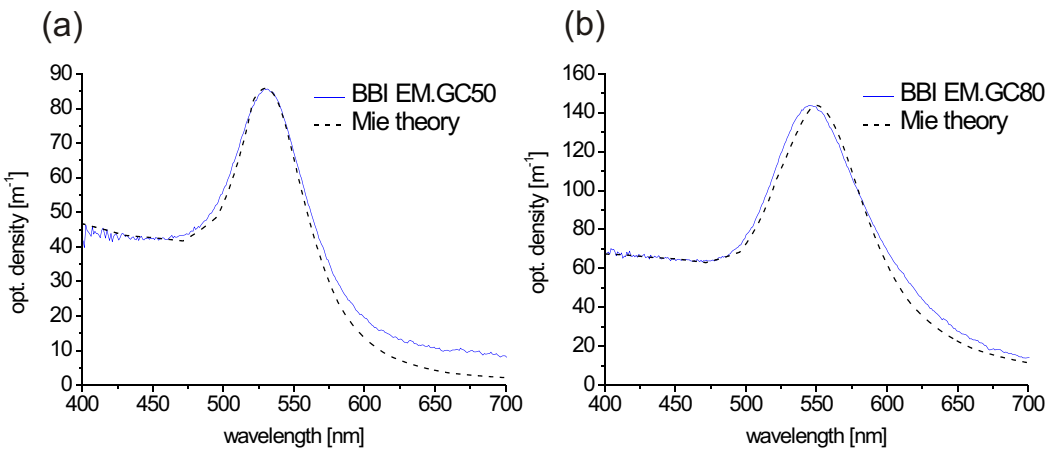


Figure 4.2: Extinction spectra recorded before the excitation experiments for (a) 50 nm (BBI EM.GC50) and (b) 80 nm (BBI EM.GC80) goldparticle suspensions in a 2 mm cell compared with the predicted curve from the Mie theory.

probelaser	50 nm		80 nm	
	OD [m ⁻¹]	T _{2mm} [%]	OD [m ⁻¹]	T _{2mm} [%]
405 nm	44	82	70	73
488 nm	48	80	67	73
561 nm	52	79	131	55
635 nm	12	95	37	84
660 nm	10	96	23	90

Table 4.1: Comparison of optical density and the corresponding transmittance of a 2 mm thick layer for the two goldparticle suspensions.

4.2 The low fluence regime

4.2.1 Results

In Fig 4.3 the optical response of 80 nm goldparticle suspensions at low excitation fluences is shown. Already slightly above the laser threshold of the Nd:YAG laser (i.e. 5 mJ/cm²) a small increase in the optical density signal can be observed at 488 nm following the excitation pulse. At a fluence of 8 mJ/cm² the two wavelengths on the red side show an optical response in the opposite direction while the extinction at 405 nm remains nearly constant (a small offset can be discerned in the noise). The duration of the signals is about 20 ns; the response in the red wavelengths is shorter and comes with a small delay to the 488 nm signal. The signal form evolves from an initially symmetric to an asymmetric shape with a rise time of 5 ns and a decay time of 20 – 25 ns. The signal amplitudes become stronger with increasing fluence until an additional drop of some nanoseconds duration appears on the signal at 488 nm (see

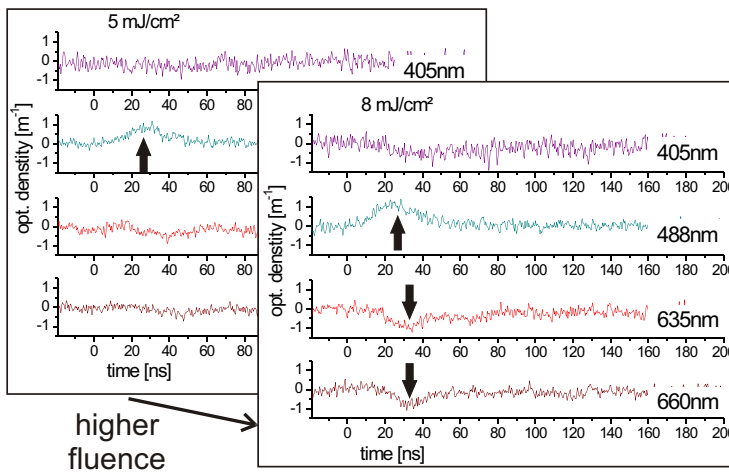


Figure 4.3: Optical response of 80 nm goldparticle suspensions in the low fluence regime. The curves have been averaged over 50 excitations. A change in the optical density of 1 m⁻¹ corresponds to a transmission change of 0.5 %.

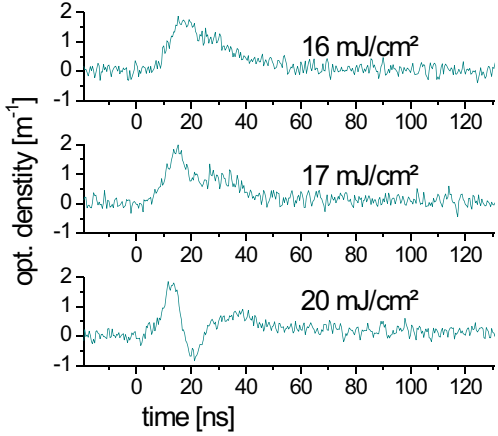


Figure 4.4: The upper graph clearly demonstrates the asymmetry of the low fluence signal at 488 nm (80 nm particle suspension). The transition to the medium fluence regime is marked by a short-term drop in the extinction that becomes more and more pronounced towards higher laser fluences.

Fig. 4.4). The appearance of this signal at 17 mJ/cm² marks the upper limit of the low fluence regime. For the 50 nm particles it was not possible to obtain reproducible signals with a comparable structure at low excitation powers.

4.2.2 Discussion

When the goldparticles are irradiated with the laser pulse, a certain part of the light is scattered and another part is absorbed (cp. Fig 2.2 on page 6). The absorbed energy leads to a heating of the particle and the surrounding fluid. The asymmetry of the signal (upper graph in Fig. 4.4) suggests a rapid heating during the laser pulse, followed by a slower decay due to heat conduction to the environment.

The impact of the heating on the extinction properties can be simulated with MiePlot using the refractive indices of bulk gold at 300 °C (from [Ott61], see also Appendix B) and the corresponding value for liquid water ($n_W^{300\text{ }^\circ\text{C}} = 1.24$ [Sch90]). The spectra and the corresponding signal changes are shown in Fig. 4.5. The simulations were performed at that particular temperature because the nucleation is reported to start around 300 °C when using nanosecond excitation [Neu05]. The qualitative behaviour of the 80 nm particle suspensions, in particular the positive extinction change in 488 nm can be reproduced. Therefore it is feasible to conclude that the optical signals reflect the temporal evolution of the temperature in and around the particle. The delayed onset of the response in the red probe beams might be explained by a different interaction range of the plasmonic oscillations with the red wavelengths “averaging” the temperature over a larger radius around the particle.

The cooling dynamics of gold nanoparticles following a sub-picosecond excitation have been studied by Hu et. al. [Hu02]. For a 50 nm particle they found a cooling time of 380 ps. If the trend of their data (a quadratic behaviour of the cooling time with respect to the particle radius) is extrapolated to 80 nm goldspheres, a

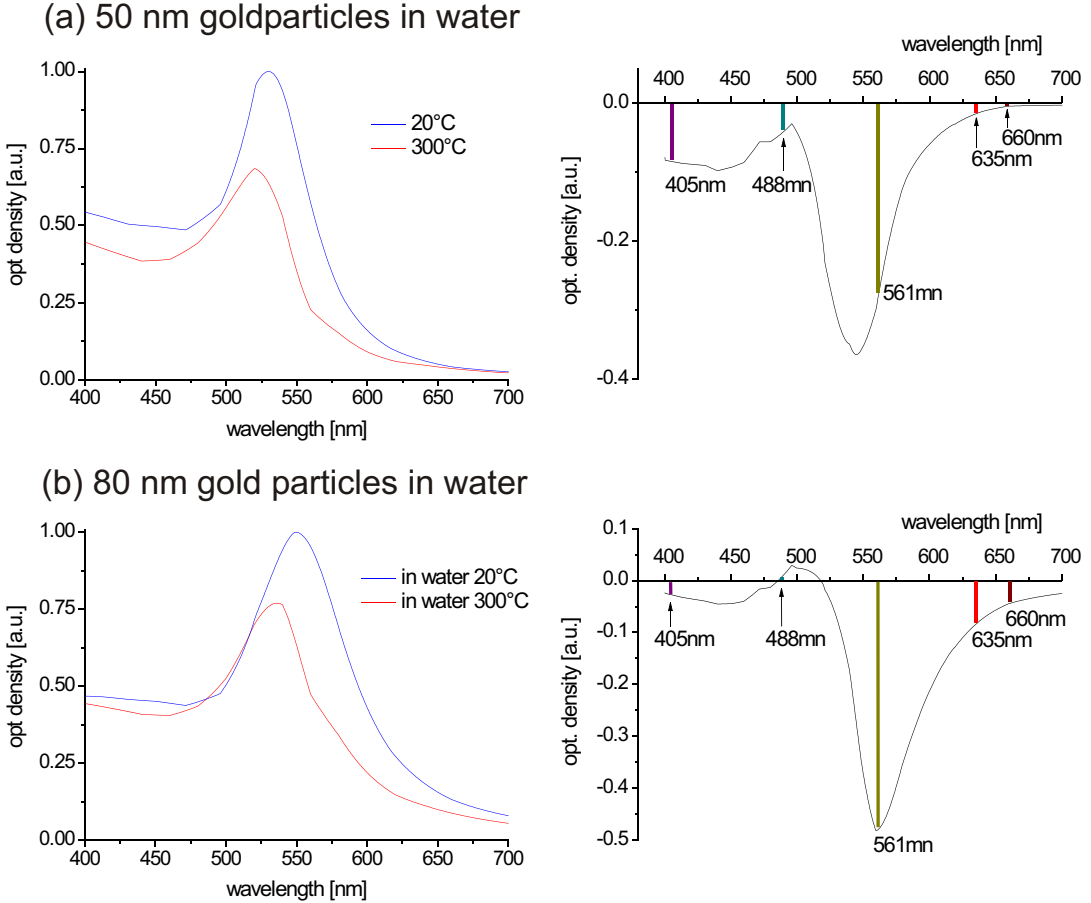


Figure 4.5: Simulated spectra for heated particles at 300 °C (left) and the corresponding signal changes. The vertical lines indicate the wavelengths of the probe lasers.

cooling time of 1000 – 1100 ps is obtained. However, the energies that are involved in their experiments are much lower than the energies in the nanosecond pulses used in this study. Moreover, the heating conditions for femtosecond excitation are adiabatic, whereas nanosecond heating means, that the particle will already heat up its environment during the laserpulse. Therefore, these timescales can be used as a lower limit for the cooling times.

For an upper limit, the cooling times of a one dimensional simulation of the heat conduction can be used. The results of a calculation of a 80 nm thick gold layer surrounded by water and irradiated by a laserpulse are presented in Appendix C. The timescale for cooling is in the order of 100 – 150 ns.

For the 50 nm particles the extinction changes are negative for all wavelengths and hence it is difficult to distinguish between low and medium fluence response.

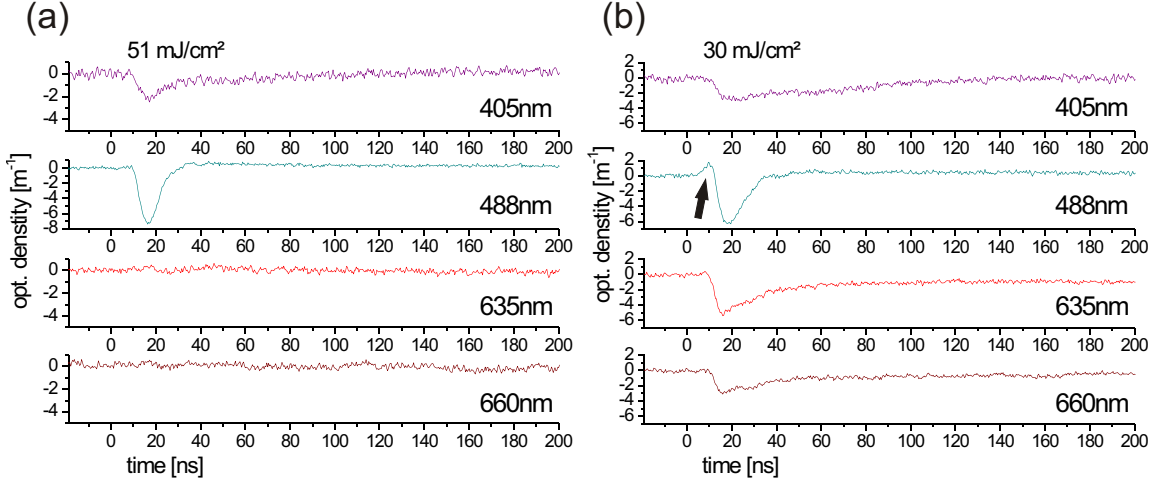


Figure 4.6: Optical density signals for (a) 50 nm and (b) 80 nm particle suspensions.

4.3 The medium fluence regime

4.3.1 Results

With increasing laser fluence the extinction drop shown in Fig. 4.4 becomes more pronounced. Fig. 4.6 shows that the response closer to the plasmon peak (i. e. 488 nm and 635 nm) is stronger than for the other wavelengths in the 80 nm particle suspension. No significant changes in the red probe beams could be observed for the 50 nm particles, whereas the blue wavelengths show a behaviour that is similar to the response of the larger particles.

Again, the signals have an asymmetric shape. The red wavelengths and the 488 nm signal show similar behaviour with short decay at a timescale of 5 ns and a recovery time to the static extinction value of 20 – 25 ns. The signal at 405 nm, however, had a relaxation time that was a factor four to five longer. Furthermore, the signal at 635 nm did not fully recover to the static optical density value. This effect becomes stronger with increasing fluence and is stable for several milliseconds.

Another remarkable feature of the signal at 488 nm for the 80 nm particles is the initial increase in optical density (black arrow in Fig. 4.6 (b)), which is a residue of the signal at the low energy regime. The signal amplitude as a function of laser fluence is shown in Fig. 4.7.

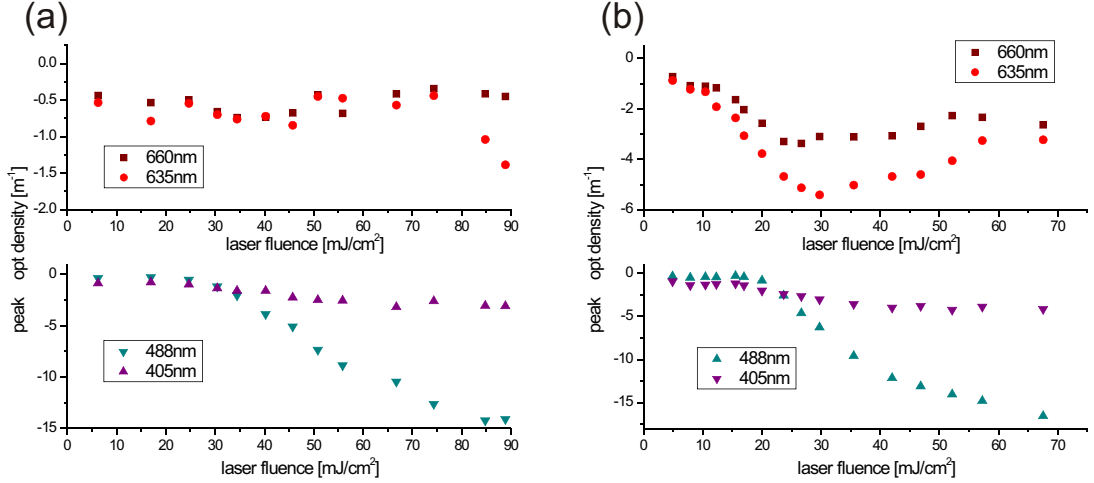


Figure 4.7: Negative peak signal as a function of excitation fluence for the red (top) and the blue probe lasers (bottom) in (a) 50 nm and (b) 80 nm goldparticle suspensions. The more or less constant value of -0.5 m^{-1} for the red wavelengths in (a) can be ascribed to the noise of the laserdiode.

4.3.2 Discussion

With increasing laser fluence, more heat is dissipated into the adjacent water layers. Eventually, boiling sets in at the surface and a steam bubble forms around the particle. This has two main consequences: first, the refractive index of the surrounding is decreased and second, the heat conduction from the particle is decreased due to the lower heat conduction coefficient of steam.

The effect on the optical properties can be simulated with MiePlot. Again, the dielectric properties of gold at 300 °C from [Ott61] (cp. Appendix B) were used. The steam has a refractive index very close to unity [Sch90], so simulations were performed assuming vacuum around the particle. The spectra and the corresponding signal changes are shown in Fig. 4.8. The vapour layer causes an extinction drop in all wavelengths with the strongest changes again being observed around the plasmon resonance. For the 50 nm particles only small changes in the red spectral range are predicted, which is confirmed by the experiment. The behaviour of the 80 nm particles in the red spectral range are in good agreement with the experiment as well. However, the simulation suggests a similar response in both of the blue probe beams, which is contrary to the experiment. The signals in the 488 nm probe beam were always stronger than the signals at 405 nm.

The increasing signal amplitude with respect to the excitation fluence can be explained by the expansion of the vapour bubble. If the steam layer around the particle is too thin, the goldsphere can still “feel” the surrounding water by means of

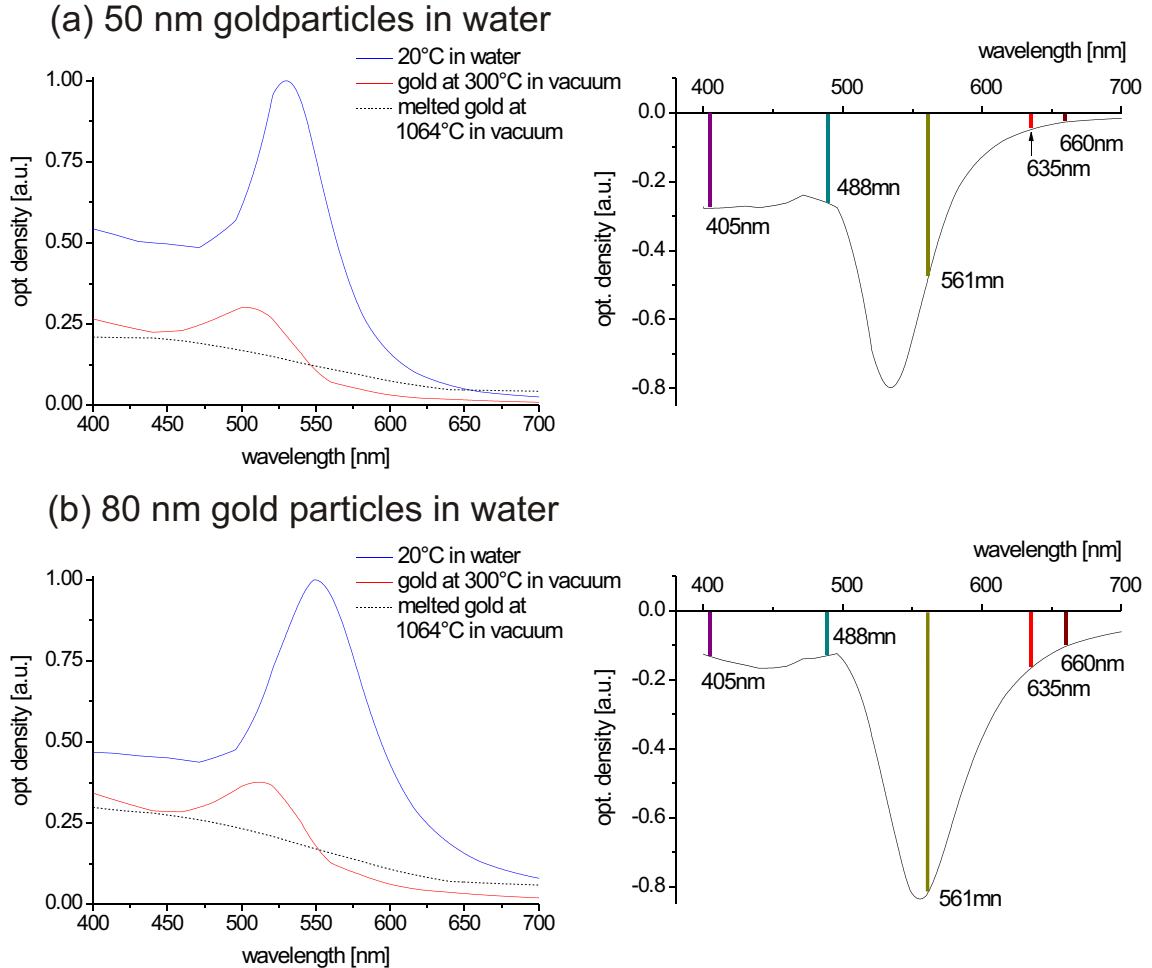


Figure 4.8: Simulated spectra for heated particles at 300 °C surrounded by vacuum (left) and the corresponding signal changes. The vertical lines indicate the wavelengths of the probe lasers.

an effective refractive index larger than one. Only if the bubble is large enough, the effect of the surrounding water can be neglected. This might account for the bends that can be seen in the signal amplitude vs. laser fluence diagram (Fig. 4.7 (b)). MiePlot only offers simulations for a sphere embedded in an infinite medium, the exact core-shell problem being difficult to calculate. In section 2.1.4(b) in [Kre95] the situation of a spherical hetero-system is discussed. According to their calculations, an additional dielectric layer covering a sodium cluster leads to a shift of the resonance, which depends on the layer thickness. In the limit of large thickness, the spectrum corresponds to the case of a sodium cluster embedded in the pure dielectric.

The formation of a vapour layer leads to a heat confinement in the particle. If this happens during the laser pulse, the heating of the particle will be accelerated and eventually it will reach its melting temperature ($T_m^{Au} = 1064\text{ }^{\circ}\text{C}$). The impact of particle melting on the optical properties have also been simulated with MiePlot (dashed line in Fig. 4.8). It shows that the plasmon peak disappears completely from the extinction spectrum. Compared to the hot solid particle, the extinction is further decreased in the blue and increased in the red spectral range. This is in good agreement with the results from Fig. 4.7.

The melting of the particle does not necessarily have to be the last step. The offset in the static extinction signal after the excitation in 635 nm (Fig. 4.6 (b)) indicates irreversible changes in the particle itself. The internal temperatures can easily reach the boiling point of the gold ($T_b^{Au} = 2856\text{ }^{\circ}\text{C}$). However, the static extinction spectra recorded after the experiments did not indicate dramatic changes following the irradiation in the medium fluence regime.

4.4 The high fluence regime

4.4.1 Results

With the advanced setup (expanded beam and thin glass cells) the maximum laser fluence was limited to the medium fluence regime. In previous studies with an unexpanded Nd:YAG beam and with 10 mm glass cells it was possible to generate another class of signals at even higher fluences. Unfortunately, in this state of the experiments the energy calibration was not yet performed by means of laser fluence at the probe volume. Only absolute pulse energies were recorded. However, this dependency should be more or less comparable to the last studies and therefore the logarithmic fit function (cp. Fig. 3.3 on page 17) was used to convert the pulse energy. These values should be proportional to the average laser fluence at the probe volume (hence the “a.u.” at the fluence axis).

At a certain fluence the extinction drop observed in the medium fluence regime was superimposed by another peak in the positive direction of some nanoseconds duration (see Fig. 4.9). The analysis of the peak heights in Fig. 4.10 shows that the amplitude keeps growing towards higher excitation fluences with the response in the blue probe signals being stronger than in the red ones. Eventually the sample becomes completely opaque (i.e. optical density $> 200\text{ m}^{-1}$; higher values for OD could not be resolved in the setup). For the 80 nm particle samples even a different threshold for the onset of the signals was observed for blue and red wavelengths.

Again, the red probe signals revealed irreversible changes in the extinction signals. They were stable for several milliseconds and a bright spot could be seen in the cells

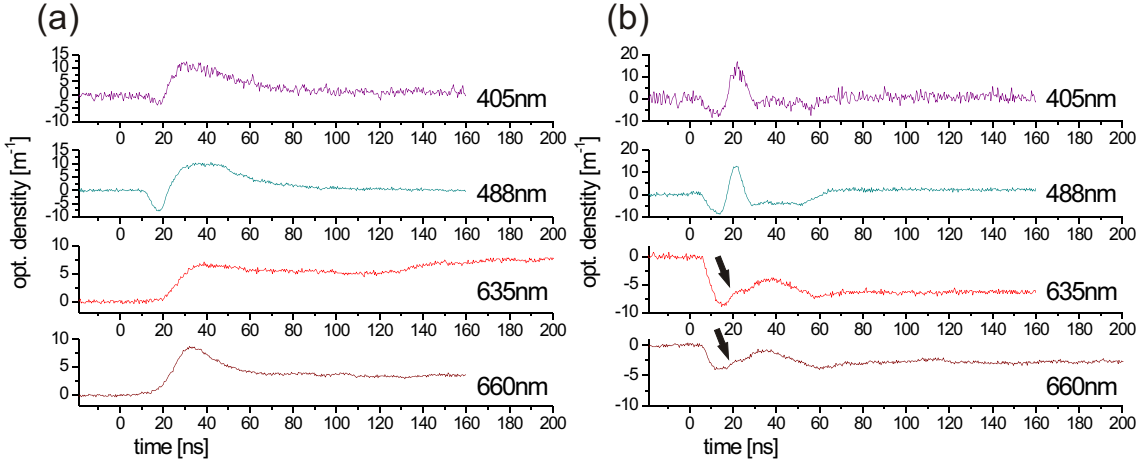


Figure 4.9: Optical density signals for (a) 50 nm and (b) 80 nm particle suspensions at the high fluence regime. The onset of the characteristic extinction peaks in (b) for the blue wavelengths can clearly be seen, while the red probe signals only reveal smallest peaks (black arrows).

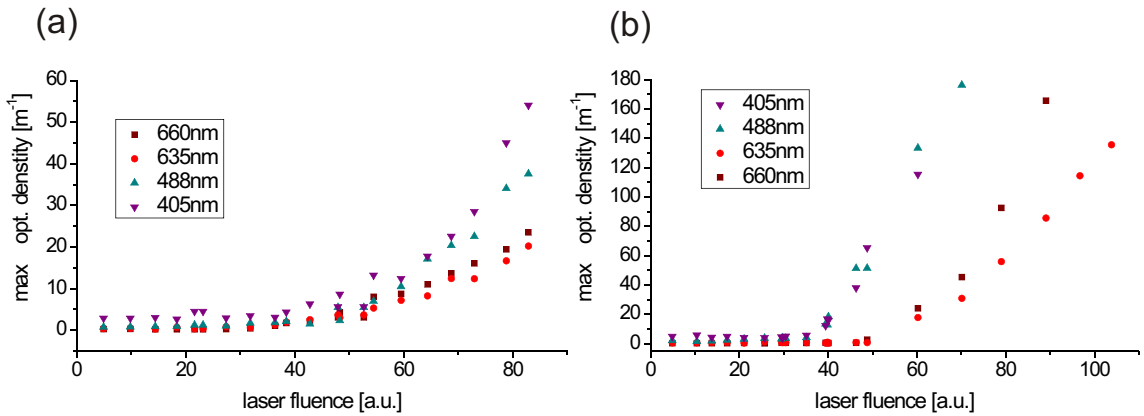


Figure 4.10: Positive peak signal as a function of excitation fluence in (a) 50 nm and (b) 80 nm goldparticle suspensions. Optical densities above 200 m^{-1} correspond to a nearly completely opaque sample.

even with the naked eye. It indicates a permanent damage of the nanospheres following the laser irradiation, which is corroborated by the extinction spectra recorded after the experiment. Fig. 4.11 shows the effect of the experiments at high fluence excitation on the spectra of the particle suspensions.

In order to avoid the accumulation of the effect on subsequent excitations, the suspensions were stirred after every irradiation.

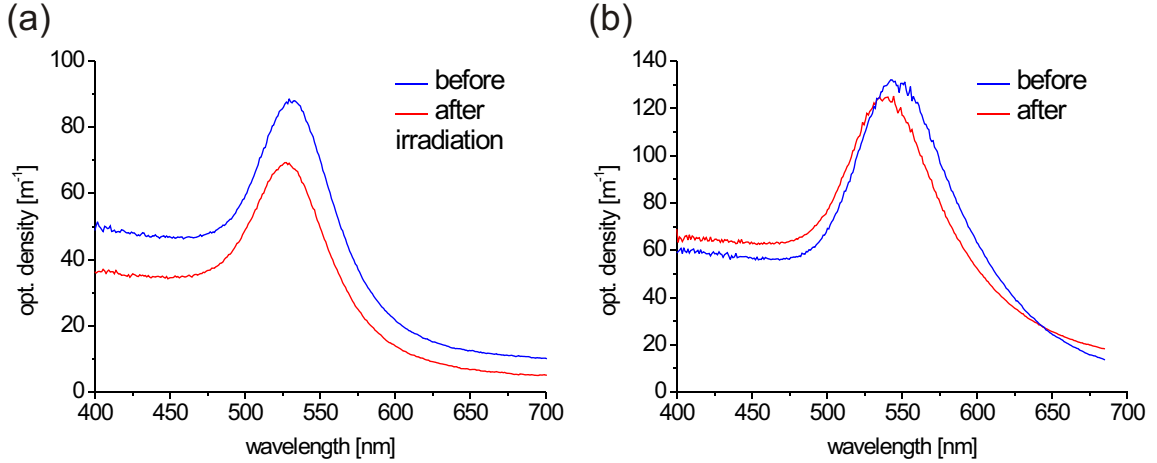


Figure 4.11: Irreversible changes by high fluence irradiation on 50 nm (a) and 80 nm particle suspensions. The blueshift of the peak position indicates a reduction of the average particle size.

A last interesting effect can be seen in Fig. 4.12, where the extinction signals in the red wavelengths show an additional drop with a duration of roughly 5 ns. The timescale of this drop does not change with higher excitation fluences and the signal does not disappear from the photodiodes if the probe lasers are turned off.

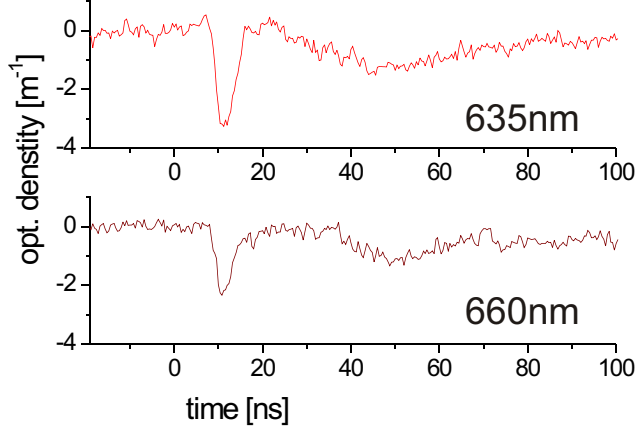


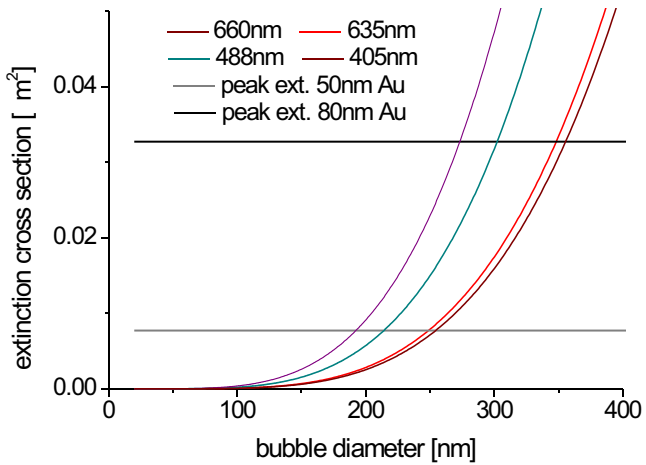
Figure 4.12: At a certain fluence, a 5 ns signal appears that does not vanish when the probe lasers are switched off. The signals depicted here were recorded at a fluence of 57 mJ/cm² (pulse energy 50 mJ).

4.4.2 Discussion

The effects that have been presented in the previous sections could all be explained by the impacts of heating and evaporation of the surrounding water on the optical properties of the goldparticle. However, the scattering behaviour of the bubbles has

been neglected so far. Fig. 4.13 shows the Mie-simulation of the extinction cross section for a steambubble as a function of its diameter for four probe wavelengths and compares it to the peak extinction cross section of an undisturbed gold particle of 50 and 80 nm diameter. The plot shows two important aspects of the problem: First, the scattering of the vapour bubbles can be neglected completely, as long as the bubbles have diameters below 100 – 150 nm. Second, the shorter wavelengths are more sensitive to bubble scattering. Hence, the signals in Fig. 4.10 clearly show the scattering behaviour that would be expected from gasbubbles in water.

Figure 4.13: Simulated extinction cross section for an airbubble in water and for comparison the peak extinction cross section of 50 nm and 80 nm goldspheres (horizontal lines). The scattering of bubbles with diameters below 100 nm is negligible. It turns out that shorter wavelengths are more sensitive to bubbles.



The signals emerging in the red wavelengths (Fig. 4.12) could be interpreted either as thermal radiation or as luminescence of the gold. According to the estimation from Sec. 2.2.2, page 9, the surface of the goldparticles emits a power of 1.4 MW/m^2 at a temperature of 3000 K. In the volume, that is irradiated by the laser (spot diameter: 5 mm, layer thickness: 2 mm, particle concentration: $\sim 10^{-16} \text{ m}^{-3}$), there are roughly $4 \cdot 10^6$ particles with an overall surface area of $8 \cdot 10^{-8} \text{ m}^2$ (spheres with diameter 80 nm). Hence, the power of the blackbody radiation from these particles is 110 mW. The distance between the sample and the photodiodes is one meter. The probe lasers are focussed onto the photodiodes by a lens (area $\sim 1 \text{ cm}^2$), so only a fraction of 10^{-5} or $1 \mu\text{W}$ reaches the photodiode. However, the peak power of the signals can be estimated to 1 – 2 mW. Therefore, thermal radiation as the origin of the signal can be ruled out.

The quantum efficiency of photoluminescence (cp. Sec. 2.2.2, page 9) is reported to be in the order of 0.01% to 0.1% [Wil98]. At the appearance of the signals, the pulse energy approximately 50 mJ. At a wavelength of 532 nm, $\sim 35\%$ of the energy is absorbed² by the particles. With a quantum efficiency of 0.1% and a pulse duration

²The transmittance of a 2 mm layer at 532 nm of the goldparticle suspension is 40% (see Fig. 4.2 on page 21); about 40% of the extinction can be ascribed to elastic scattering.

of 10 ns, the power of the luminescence radiation at the sample would be 180 W or 1.8 mW at the photodiode, which is very close to the observed effect.

If the signals are caused by luminescence, they will have a characteristic spectrum in the red and infrared spectral range [Bev03]. A first indication towards a broadband character of the signals is that they could only be observed, when the photodiodes for the red probe beams were equipped with an edge filter (i.e. all wavelengths below a certain value, 600 nm in this case, are blocked). The signals disappeared when an additional narrowband interference filter was used.

4.5 Experiments with uv-excitation and a yellow probe laser

The results and their interpretation from the previous sections have demonstrated the complex correlation of local temperature distribution and the optical properties of gold nanoparticles. It turned out that the plasmon resonance wavelength is already shifted during the excitation pulse. The wavelength of 532 nm was initially chosen to ensure a sufficiently high absorption in the sample. However, this absorption is not constant during the laserpulse. Thus, the excitation should be performed in a spectral range, where the absorption is less affected by temperature changes. The third harmonic of the Nd:YAG laser has a wavelength of 355 nm, which is in the rather stable interband absorption regime of the gold spectrum. Moreover, the simulations in Fig. 4.5 and 4.8 have shown, that the laser-induced shifts are most prominent in the spectral range between 500 and 600 nm. These considerations led to the implementation of a last experiment with a frequency-tripled Nd:YAG and an additional probelaser at a wavelength of 561 nm. First results on 80 nm goldparticle suspensions are displayed in Fig. 4.14. They are still lacking an appropriate energy calibration, hence the graphs are labelled with the pulse energy of the reflection of a glass slide in the Nd:YAG-beam (cp. Fig. 3.1 on page 16).

A main result of this study is an enormous boost in sensitivity due to the use of the 561 nm probe laser. It clearly corroborates the simulations from Fig. 4.5 and Fig. 4.8. The characteristic signals from the low and the medium fluence regimes could be reproduced. The transition between the two regimes is clearly visible in 4.14(b) (black arrow). The longer relaxation times for the signal at 405 nm, observed in 4.6 on page 25, could not be reproduced. Finally, at the highest excitation powers, the transition to bubble-dominated extinction was observed. Again, the short wavelengths showed a stronger response than the longwave signals.

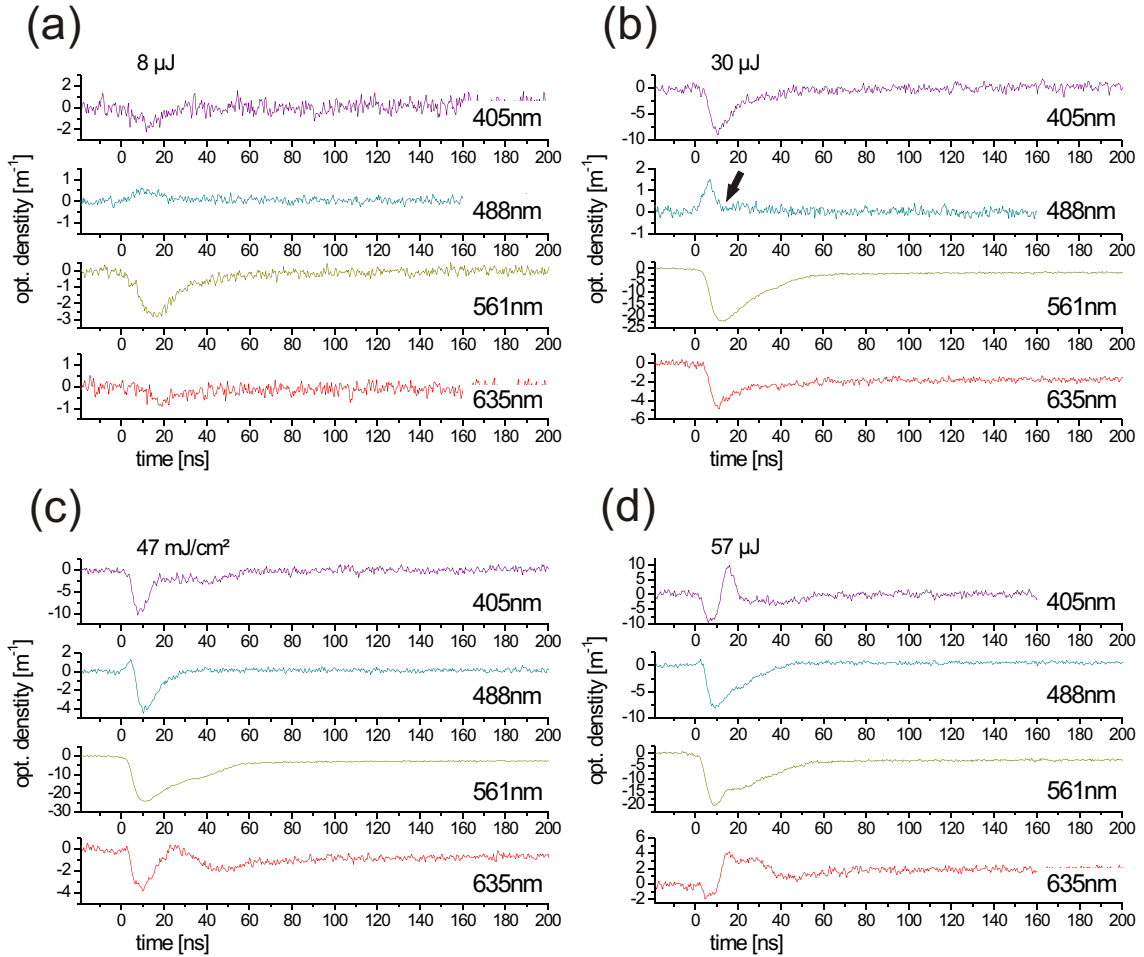


Figure 4.14: First results of experiments performed with uv-excitation on 80 nm goldparticle suspensions and a 561 nm probe laser. The main features of the previous studies can be reproduced: the low fluence (a) and medium fluence (b) regime and the transition between them (c). Furthermore the signals at high excitation energies shows the characteristic bubble dominated scattering behaviour of the high fluence regime (d).

5 Outlook

From the results of the time resolved extinction measurements a detailed mechanism for the dissipation of a nanosecond laserpulse could be inferred. However there are still many open questions regarding experimental issues and the interpretation of the signals.

Theoretical questions

- With the Mie theory the signals were interpreted qualitatively. However the quantitative response cannot be explained by a simple combination of temperature dependent bulk dielectric functions of medium and sphere. The water pressure at the surface of the particle, especially when the bubble nucleation sets in, will also play an important role. With the formation of a vapour layer around the particle, the system acts like a core-shell system, which is even more difficult to model.
- The dynamics of the heat transfer upon nanosecond heating have not been simulated satisfactorily, so far. Especially the time dependent absorption during the laser pulse will be difficult to take into account. A possible approach would be to extend the algorithm of Jörg Bischof (see [Bis96] and Appendix C) to a spherical symmetric situation, e.g. by an increasing heat capacity of layers, that are further away from the centre of the particle.

Experimental tasks

- The first experiments with an excitation wavelength of 355 nm have provided comparable results to the previous studies at 532 nm. Compared to the plasmon dominated green spectral range, the ultraviolet optical properties of the gold nanoparticles are dominated by interband absorption. Hence, they are less affected by the temperature changes during the excitation pulse. Comparison with simulations assuming a constant absorption rate for the pulsed laser, that are easier to implement, would be possible.
- A very important issue for the comparability of the results is the energy calibration. The setup for the uv excitation still lacks an appropriate cali-

bration measurement. Furthermore, the method with the pinhole should be compared with other methods, such as the melting dynamics of a germanium surface¹ [Bon93].

- The strongest relative extinction changes are expected in the green and yellow spectral range. With an excitation wavelength in the ultraviolet it is now possible to study the optical properties in that particular range. First experiments with a 561 nm probelaser already demonstrated an immense boost in sensitivity. Another alternative would be a continuous wave Nd:YAG at 532 nm.
- As a result of the heating, the Mie calculation for the low fluence regime predicted an increased extinction for the 80 nm goldparticles in the spectral range from 485 nm up to 518 nm (cp. Fig. 4.5 on page 24) in contrast to an extinction drop for all other visible wavelengths. The emission of the argon-ion laser can be adjusted to different wavelengths in that range (476.5 nm, 488.0 nm, 496.5 nm, 501.7 nm, 514.5 nm and 528.7 nm). Using these wavelengths, the predictions of the Mie theory can be tested.
- The influence of the particle size on the nanoscale heat transfer properties would be another parameter worth studying. Changing the particle material could bear some experimental problems, viz. the nonexistence of a plasmon resonance in the visual spectral range.
- The experiments have shown that the plasmon resonance is very sensitive to changes in the particle and its environment. Hence, the time resolved extinction of gold nanoparticle suspensions acts like a thermometer for the nanoscale heat transfer. With an appropriate theoretical model it is possible to control the thermodynamic conditions both in and around the particle. An interesting application would be to use goldparticles as microreactors. At controlled temperatures, chemical reactions or phase transitions in surface bound molecular layers could be stimulated.

¹The threshold fluence for surface melting of germanium at ns-illumination is 100 mJ/cm², which is at the upper end of the fluence scale for the measurements in Sec. 4.3

Summary

For the first time in this group, bubble nucleation was studied at nanoscopic interfaces, namely on the surface of gold nanoparticles suspended in water. Their plasmonic properties proved to be a very sensitive indicator for dielectric modifications both in and around the particles. By probing at four wavelengths simultaneously, the impact of an excitation by a pulsed laser on the optical properties could be studied close to the plasmon resonance (488 nm, 561 nm¹ and 635 nm) as well as in the interband absorption regime (405 nm) and the longwave shoulder of the plasmon peak (660 nm). From the comparison of the time-resolved extinction measurements on 50 nm and 80 nm goldparticle suspensions with Mie simulations including the temperature dependent bulk dielectric functions of both the particle and matrix material, the mechanism of bubble nucleation around the particles could be inferred.

Already moderate excitation powers give rise to changes in the absorbance of the samples, which are being ascribed to changes in the optical properties caused by the heating of the particle and its environment (*low fluence regime*). The formation of a vapour layer around the particle at higher excitation fluences leads to a decoupling of the plasmonic oscillations in the electron gas of the particle from the dielectric of the surrounding water layers (*medium fluence regime*). This results in a extinction drop in the whole visible spectral range. The formation of the bubble at a certain threshold fluence is clearly visible in the signal of the 488 nm probe laser, where the response ascribed to the heating (an extinction increase) is complementary to the extinction drop due to the bubble. With increasing excitation fluence, the bubbles become larger and eventually, the scattering properties of the bubbles become dominant. The extinction at this *high fluence regime* clearly reflects the scattering behaviour that would be expected from vapour bubbles, viz. a stronger scattering in shorter wavelengths. Finally the sample became completely opaque for some nanoseconds, showing an Optical Limiting behaviour.

A first experiment demonstrated that the sensitivity of the setup can be increased by utilizing probe wavelengths closer to the plasmon peak. Furthermore, the excitation wavelength was shifted to the ultraviolet, where the absorption is more stable throughout the laser pulse. The main features of the previous studies could be reproduced. Moreover, the prediction by the Mie theory of a highly increased optical response in the green and yellow spectral rage was corroborated.

¹With the 561 nm laser only one last experiment was performed (see Sec. 4.5).

Appendix A

Mie theory

In this section the basic ideas of the Mie theory are introduced. The description follows the notation of [Boh83], where the complete derivations can be found.

The first step is to describe the incoming electromagnetic wave in spheric coordinates with the sphere placed in the origin. The electric field can be described by

$$\vec{E}_i(r, \vartheta, \varphi) = E_0 \sum_{n=1}^{\infty} i^n \frac{2n+1}{n(n+1)} (M_n^{(1)}(r, \vartheta, \varphi) - i N_n^{(1)}(r, \vartheta, \varphi)). \quad (\text{A.1})$$

The vector functions $M_n^{(0)}(r, \vartheta, \varphi)$ and $N_n^{(0)}(r, \vartheta, \varphi)$ are called vector spherical harmonics. They have to be chosen in a way that they satisfy the electromagnetic wave equation. They turn out to have the form $\{\text{trigonometric function}\} \cdot \{\text{spherical Bessel function}\} \cdot \{\text{Legendre function}\}$. The corresponding magnetic fields H_i can be derived from (A.1) using the Maxwell equations. At the surface of the sphere, the boundary condition has to be fulfilled :

$$(\vec{E}_i + \vec{E}_s - \vec{E}_{int}) \times \vec{e}_r = (\vec{H}_i + \vec{H}_s - \vec{H}_{int}) \times \vec{e}_r = 0 \quad (\text{A.2})$$

The indices i , s and int stand for the incident, the scattered and the internal fields, respectively. They can be described in the form

$$\vec{E}_{int} = E_0 \sum_{n=1}^{\infty} i^n \frac{2n+1}{n(n+1)} (c_n M_n^{(1)} - id_n N_n^{(1)}), \quad (\text{A.3a})$$

$$\vec{H}_{int} = \frac{-k_{int}}{\omega \mu_{int}} \sum_{n=1}^{\infty}, i^n \frac{2n+1}{n(n+1)} (d_n M_n^{(1)} - ic_n N_n^{(1)}), \quad (\text{A.3b})$$

$$\vec{E}_s = E_0 \sum_{n=1}^{\infty} i^n \frac{2n+1}{n(n+1)} (ia_n N_n^{(0)} - b_n M_n^{(3)}), \quad (\text{A.3c})$$

$$\vec{H}_s = \frac{-k}{\omega \mu} \sum_{n=1}^{\infty} i^n \frac{2n+1}{n(n+1)} (ia_n N_n^{(0)} - b_n M_n^{(3)}), \quad (\text{A.3d})$$

Appendix A Mie theory

where k_{int} and k are the wavenumbers and μ_{int} and μ the permeabilities¹ inside and outside the sphere, respectively. The spherical harmonics are multiplied with complex functions a_n , b_n , c_n and d_n called *scattering coefficients*. The functions c_n and d_n are of no further interest, as they only describe the internal field of the particle. The other coefficients are found to be

$$a_n = \frac{m\Psi_n(mx)\psi'_n(x) - \Psi_n(x)\psi'_n(mx)}{m\Psi_n(mx)\xi'_n(x) - \xi_n(x)\psi'_n(mx)} \quad (\text{A.4a})$$

$$b_n = \frac{\Psi_n(mx)\psi'_n(x) - m\Psi_n(x)\psi'_n(mx)}{\Psi_n(mx)\xi'_n(x) - m\xi_n(x)\psi'_n(mx)}, \quad (\text{A.4b})$$

with the *relative refractive index* $m = n_0(\omega)/n_m$, the ratio of the frequency dependent refractive index of the sphere to the refractive index of the surrounding medium and the *size parameter* $x = \frac{2\pi}{\lambda} R n_m$, where R denotes the particle radius. The *Riccati-Bessel functions* $\psi'_n(x) = xj_n(x)$ and $\xi'_n(x) = xh_n(x)$ are derived from the spheric Bessel function of *first kind* $j_n(x)$ and *third kind* $h_n(x)$, respectively. With ψ' the first derivative with respect to the whole argument in parentheses is meant. In order to get information about how much energy is taken from the incident planar wave, the Poynting vector $\vec{S} = \vec{E} \times \vec{H}$ of the resulting electromagnetic field has to be integrated over a closed surface around the sphere, which is sufficiently far away in order to avoid near field effects:

$$W = - \oint \vec{S} \cdot \vec{n} dA. \quad (\text{A.5})$$

\vec{n} is the outward pointing surface normal vector (hence the " - " sign). The resulting Poynting vector can be written as $\vec{S} = \vec{S}_i + \vec{S}_{sca} + \vec{S}_{ext}$, where \vec{S}_i and \vec{S}_{sca} are the components of the incident and scattered wave. \vec{S}_{ext} contains the mixed terms and can be interpreted as the total energy loss of the incident wave after the particle (*ext* for *extinction*). Furthermore, the energy flux of a planar wave through a closed surface will be zero. Hence the contribution of the undisturbed incident wave will be zero. This leads to the equation for the nonradiative energy loss:

$$W_{abs} = W_{ext} - W_{sca}. \quad (\text{A.6})$$

¹Usually they are assumed to be unity for optical frequencies.

The corresponding cross sections can be obtained by normalizing the different contributions by the *irradiance* I_i of the incident field (dimensions: energy per area and time):

$$\sigma_{sca} = \frac{W_{sca}}{I_i} = \frac{2\pi}{k^2} \sum_{n=1}^{\infty} (2n+1) (|a_n|^2 + |b_n|^2) \quad (\text{A.7a})$$

$$\sigma_{ext} = \frac{W_{ext}}{I_i} = \frac{2\pi}{k^2} \sum_{n=1}^{\infty} (2n+1) \operatorname{Re} \{a_n + b_n\} \quad (\text{A.7b})$$

These equations are the basis for the calculation of the extinction spectra as they are used in this work. Additionally, the dielectric functions of the sphere material and the medium are required (bulk values are sufficient; see discussion in chapter 2.1.2). For every frequency ω the scattering coefficients (A.4) of the first significant orders are computed. Here the size parameter $x = \frac{2\pi}{\lambda} R n_m$ can act as a stop criterion: for $n > x$ the contributions become negligible. An example for a complete computation algorithm is the BHMIE - algorithm, which is used in the freeware software MiePlot [Lav06]. It is described in Chapter 4 and Appendix A of [Boh83].

Appendix B

Temperature dependent optical constants of gold

The Mie-simulation software MiePlot [Lav06] requires the wavelength dependent complex refractive indices of the particle material. The standard source for the optical constants of noble metals is a paper by Johnson and Christy [Joh72]. However, they only studied gold at room temperature. For temperature dependent values the data from Otter [Ott61] can be used. Unfortunately, the data is only available in the form a single plot (Fig. B.1). The relations between dielectric constants ϵ_1 and ϵ_2 and the complex refractive indices n and k are given by

$$\epsilon_1 + i\epsilon_2 = (n + ik)^2 \quad (\text{B.1})$$

$$\Rightarrow k = \sqrt{\frac{1}{2} \left(\sqrt{\epsilon_1^2 + \epsilon_2^2} - \epsilon_1 \right)} \quad (\text{B.2})$$

$$\Rightarrow n = \frac{\epsilon_2}{2k} \quad (\text{B.3})$$

The following tables will give both the dielectric constants and the corresponding refractive indices for wavelengths between 440 nm and 640 nm from the plot. Additional values for 400 nm and 700 nm have been extrapolated in order to get information for the probelaser wavelengths at 405 nm and 660 nm.

Appendix B Temperature dependent optical constants of gold

wavelength [nm]	$-\epsilon_1$	ϵ_2	n	k
400	1,1*	6,8*	1,7*	2*
440	1,12	6	1,58	1,9
460	1,31	5,45	1,47	1,86
480	1,84	4,57	1,24	1,84
500	2,76	3,69	0,96	1,92
520	4,08	2,94	0,69	2,13
540	5,52	2,47	0,51	2,4
560	7,69	2,16	0,39	2,8
580	8,62	1,95	0,33	2,95
600	10	1,74	0,27	3,17
620	11,64	1,71	0,25	3,42
640	13,03	1,92	0,27	3,62
700	17,2*	2,55*	0,31*	4,16*

Table B.1: Optical constants of gold at 310 °C. Values with an asterisk are extrapolated.

wavelength [nm]	$-\epsilon_1$	ϵ_2	n	k
400	0,5*	7,5*	1,87*	2*
440	1,31*	6,8*	1,68*	2,03*
460	1,84*	6,25*	1,53*	2,04*
480	2,36	5,8	1,4	2,08
500	3,2	5,01	1,17	2,14
520	4,08	4,62	1,02	2,26
540	5,07	4,05	0,84	2,4
560	6,7	3,82	0,71	2,68
580	7,9	3,56	0,62	2,88
600	9,5	3,4	0,54	3,13
620	10,52	3,3	0,5	3,28
640	11,8*	3,25*	0,47*	3,47*
700	15,64*	3,1*	0,39*	3,97*

Table B.2: Optical constants of solid gold at the melting point of 1064 °C. Values with an asterisk are extrapolated.

wavelength [nm]	$-\epsilon_1$	ϵ_2	n	k
400	0,5*	7,69*	1,96*	1,96*
440	1,84*	6,88*	1,85*	1,85*
460	2,5*	6,77*	1,84*	1,84*
480	3,42	6,66	1,82	1,82
500	4,21	6,55	1,81	1,81
520	5	6,44	1,79	1,79
540	5,92	6,33	1,78	1,78
560	6,71	6,22	1,76	1,76
580	7,63	6,13	1,75	1,75
600	8,82	6,13	1,75	1,75
620	10	6,13	1,75	1,75
640	11,31*	6,13*	1,75*	1,75*
700	15,24*	6,13*	1,75*	1,75*

Table B.3: Optical constants of liquid gold at the melting point of 1064 °C. Values with an asterisk are extrapolated.

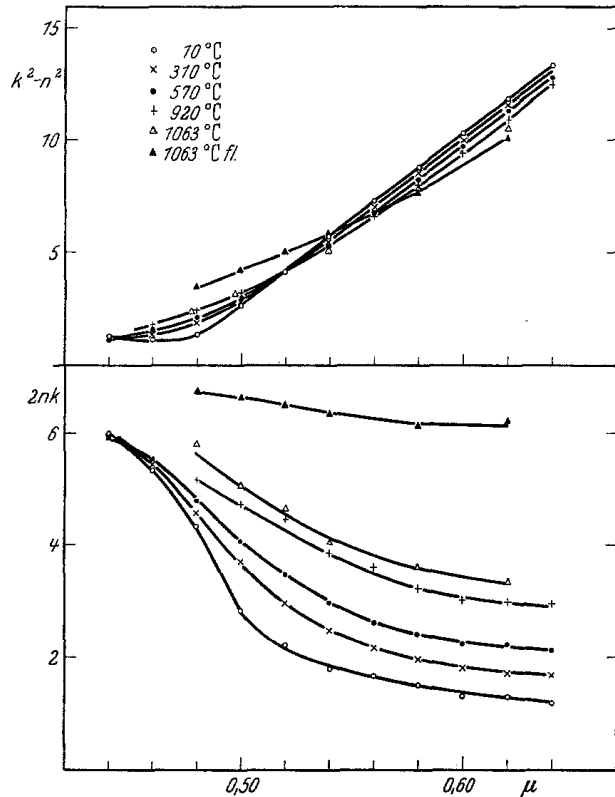


Figure B.1: Graph from [Ott61].

The plots show the dielectric constants for different temperatures: $-\epsilon_1$ (upper graph) and ϵ_2 (lower graph).

Appendix C

One dimensional heat transfer

Three dimensional heat transfer, even in spherically symmetric geometry, is very difficult to simulate. Unfortunately no analytical solution to the problem has been found so far. A half analytical solution was proposed by Goldenberg [Gol52] and Cooper [Coo77]. A big effort has been carried out towards numerical solutions. However, even applying these formula to rectangular heating pulse is very time consuming, not to mention a gaussian pulse profile.

Within the scope of his dissertation Jörg Bischof developed a software for the simulation of the one dimensional heat transfer from a laser illuminated surface [Bis96]. It utilizes the method of finite differences, where the system is split in a finite number of layers with defined thermodynamic properties. For interfaces between different materials, the thermal boundary resistance can be included. Of course, in the one dimensional case plasmonic contributions to the absorption in the film are neglected. The timescales from these simulations can be used as a upper limit of the timescale the three dimensional problem. In Fig. C.2 the simulation of the temperature in and around a 80 nm thick gold film surrounded by water is shown. For the thermal boundary resistance of the water-gold interface a value of $100 \text{ MJ/m}^2\text{K}$ was used [Ple04, Wil02]. The excitation source was a 532 nm, 9 ns FWHM light pulse at a power of 50 mJ/cm^2 . The initial temperature was set to room temperature (293 K).

The decay times for the temperature are in the order of 100 – 150 ns. The peak temperature is reached with a little delay to the peak of the excitation pulse, which is prolonged for more distant water layers. A residual temperature increase of 10 – 20 K remaines for at least 500 ns.

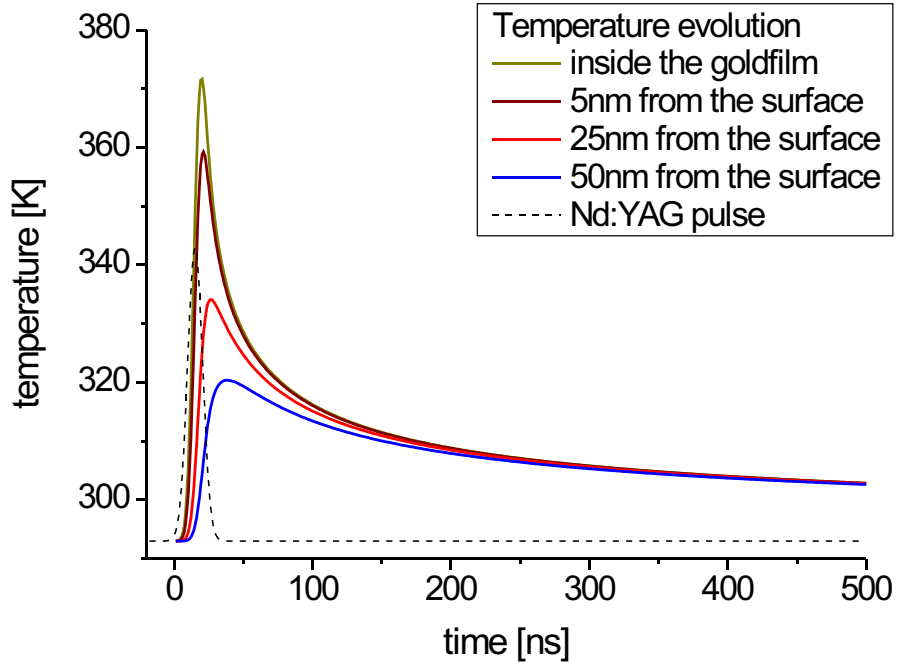


Figure C.1: Simulated heat transfer from a 80 nm gold film to the surrounding water layers.

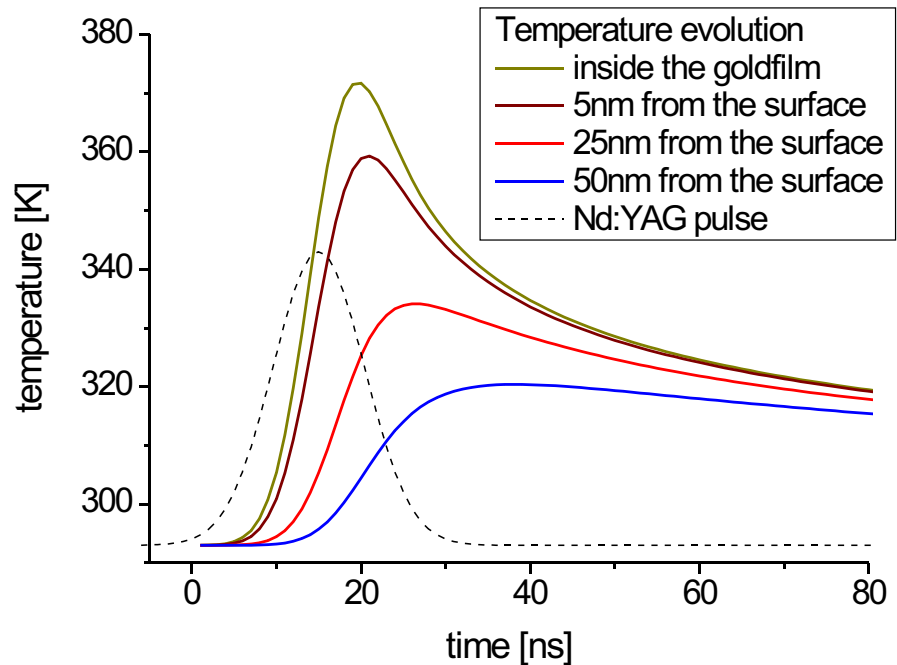


Figure C.2: Detail of the first 80 ns of the simulated heat transfer.

Bibliography

- [Bev03] M. R. Beversluis, A. Bouhelier and L. Novotny, *Continuum generation from single gold nanostructures through near-field mediated intraband transitions*, Phys. Rev. B **68**(11), p. 115433 (2003), url/doi: [10.1103/PhysRevB.68.115433](https://doi.org/10.1103/PhysRevB.68.115433). 9, 32
- [Bis96] J. Bischof, *Metallisches Dünnefilmschmelzen nach Pulslaser-Bestrahlung: Phasenumwandlung und Instabilitäten*, Dissertation, Universität Konstanz (1996). 35, 47
- [Boh83] C. Bohren and D. Huffmann, *Absorption and scattering of light by small particles*, John Wiley & Sons, Inc. (1983). 39, 41
- [Bon93] J. Boneberg, *Dynamik der Verfestigung von Halbleiterschichten nach ns-Laser-Annealing*, Dissertation, Universität Konstanz (1993). 36
- [Boy86] G. T. Boyd, Z. H. Yu and Y. R. Shen, *Photoinduced luminescence from the noble metals and its enhancement on roughened surfaces*, Phys. Rev. B **33**(12), p. 7923 (1986), url/doi: [10.1103/PhysRevB.33.7923](https://doi.org/10.1103/PhysRevB.33.7923). 9
- [Car59] H. Carslaw and J. Jaeger, *Conduction of heat in solids*, Oxford University Press (1959). 8
- [Coo77] F. Cooper, *Heat transfer from a sphere to an infinite medium*, Int. J. Heat Mass Tran. **00**, p. 991 (1977). 47
- [Dah06] C. Dahmen, *Optische und strukturelle Eigenschaften von Edelmetall-nanopartikeln*, Dissertation, Rheinisch-Westfälische Technische Hochschule Aachen (2006). 6
- [Dob01] V. Dobler, *Dynamische Messungen zum Laser-Cleaning*, Dissertation, Universität Konstanz (2001). 2
- [Fat00] N. Fatti, C. Voisin, M. Achermann, S. Tzortzakis, D. Christofilos and F. Vallée, *Nonequilibrium electron dynamics in noble metals*, Phys. Rev. B **61**(24), p. 16956 (2000), url/doi: [10.1103/PhysRevB.61.16956](https://doi.org/10.1103/PhysRevB.61.16956). 7
- [Fat01] N. D. Fatti and F. Vallée, *Ultrafast optical nonlinear properties of metal nanoparticles*, Appl. Phys. B **73**, p. 383 (2001), url/doi: <http://www.springerlink.com/content/d626kb9tgelr8anp/>. 7

Bibliography

- [Fra00] L. Francois, M. Mostafavi, J. Belloni, J.-F. Delouis, J. Delaire and P. Feneyrou, *Optical limitation induced by gold clusters. 1. size effect*, J. Phys. Chem. B **104**(26), p. 6133 (2000), url/doi: 10.1021/jp9944482. 2
- [Fra01] L. Francois, M. Mostafavi, J. Belloni and J. A. Delaire, *Optical limitation induced by gold clusters: Mechanism and efficiency*, Phys. Chem. Chem. Phys. **3**(22), p. 4965 (2001), url/doi: 10.1039/b106690k. 2
- [Gol52] H. Goldenberg and C. J. Tranter, *Heat flow in an infinite medium heated by a sphere*, Brit. J. Appl. Phys. **3**(9), p. 296 (1952), url/doi: <http://stacks.iop.org/0508-3443/3/296>. 47
- [Har04] G. V. Hartland, *Measurements of the material properties of metal nanoparticles by time-resolved spectroscopy*, Phys. Chem. Chem. Phys. **6**(23), p. 5263 (2004), url/doi: 10.1039/b413368d. 7, 12
- [Har06] G. V. Hartland, *Coherent excitation of vibrational modes in metallic nanoparticles*, Annu. Rev. Phys. Chem. **57**(1), p. 403 (2006), url/doi: 10.1146/annurev.physchem.57.032905.104533. 7, 11
- [Hu02] M. Hu and G. Hartland, *Heat dissipation for au particles in aqueous solution: Relaxation time versus size*, J. Phys. Chem. B **106**(28), p. 7029 (2002), url/doi: 10.1021/jp020581. 7, 23
- [Ime91] K. Imen, S. J. Lee and S. D. Allen, *Laser-assisted micron scale particle removal*, Appl. Phys. Lett. **58**(2), p. 203 (1991), url/doi: 10.1063/1.104923. 2
- [Ina06] S. Inasawa, M. Sugiyama, S. Noda and Y. Yamaguchi, *Spectroscopic study of laser-induced phase transition of gold nanoparticles on nanosecond time scales and longer*, J. Phys. Chem. B **110**(7), p. 3114 (2006), url/doi: 10.1021/jp0571751. 12, 13
- [Jac99] J. Jackson, *Classical Electrodynamics*, John Wiley & Sons, Inc., 3 Auflage (1999). 3
- [Joh72] P. B. Johnson and R. W. Christy, *Optical constants of the noble metals*, Phys. Rev. B **6**(12), p. 4370 (1972), url/doi: 10.1103/PhysRevB.6.4370. 43
- [Kot06] V. Kotaidis, C. Dahmen, G. von Plessen, F. Springer and A. Plech, *Excitation of nanoscale vapor bubbles at the surface of gold nanoparticles in water*, J. Chem. Phys. **124**(18), p. 184702 (2006), url/doi: <http://link.aip.org/link/?JCP/124/184702/1>. 9, 11
- [Kre95] U. Kreibig and M. Vollmer, *Optical properties of metal clusters*, Springer-Verlag Berlin Heidelberg (1995). 4, 6, 27

- [Kri90] S. Krishnan, G. P. Hansen, R. H. Rauge and J. L. Margrave, *Spectral emissivities and optical properties of electromagnetically levitated liquid metals as functions of temperature and wavelength*, High Temp. Sci. **26**, p. 143 (1990). 10
- [Kur98] H. Kurita, A. Takami and S. Koda, *Size reduction of gold particles in aqueous solution by pulsed laser irradiation*, Appl. Phys. Lett. **72**(7), p. 789 (1998), url/doi: <http://link.aip.org/link/?APL/72/789/1>. 9, 12
- [Lan02] F. Lang, *Steam Laser Cleaning von Siliziumwafern*, Diplomarbeit, Universität Konstanz (2002). 2
- [Lan04] F. Lang, P. Leiderer and S. Georgiou, *Phase transition dynamics measurements in superheated liquids by monitoring the ejection of nanometer-thick films*, Appl. Phys. Lett. **85**(14), p. 2759 (2004), url/doi: [10.1063/1.1803618](https://doi.org/10.1063/1.1803618). 2
- [Lan06] F. Lang, *Liquid-Vapor Phase Transitions at Solid Surfaces*, Dissertation, Universität Konstanz (2006). 2, 10, 11
- [Lap06] D. Lapotko, E. Lukianova, M. Potapnev, O. Aleinikova and A. Oraevsky, *Method of laser activated nano-thermolysis for elimination of tumor cells*, Cancer Letters **239**(1), p. 36 (2006), url/doi: [10.1016/j.canlet.2005.07.031](https://doi.org/10.1016/j.canlet.2005.07.031). 2
- [Lav06] P. Laven, *Mieplot v3.5.01*, <http://www.philiplaven.com/mieplot.htm> (2006). 5, 6, 41, 43
- [Lin00] S. Link, C. Burda, B. Nikoobakht and M. El-Sayed, *Laser-induced shape changes of colloidal gold nanorods using femtosecond and nanosecond laser pulses*, J. Phys. Chem. B **104**(26), p. 6152 (2000), url/doi: [10.1021/jp000679t](https://doi.org/10.1021/jp000679t). 9
- [Mat99] R. Matzdorf, A. Gerlach, F. Theilmann, G. Meister and A. Goldmann, *New lifetime estimates for d-band holes at noble metal surfaces*, Appl. Phys. B **68**, p. 393 (1999). 7
- [Mie08] G. Mie, *Beiträge zur optik trüber medien, speziell kolloidaler metallösungen*, Annalen der Physik **330**(3), p. 377 (1908). 5
- [Moo69] A. Mooradian, *Photoluminescence of metals*, Phys. Rev. Lett. **22**(5), p. 185 (1969), url/doi: [10.1103/PhysRevLett.22.185](https://doi.org/10.1103/PhysRevLett.22.185). 9
- [Mos00] M. Mosbacher, V. Dobler, J. Boneberg and P. Leiderer, *Universal threshold for the steam laser cleaning of submicron spherical particles from silicon*, Appl. Phys. A **70**(6), p. 669 (2000). 2

Bibliography

- [Neu03] J. Neumann and R. Brinkmann, *Microbubble dynamics around laser heated microparticles*, in R. W. Steiner (Herausgeber), *Proc. SPIE*, Band 5142, p. 82–87, SPIE (2003), url/doi: 10.1117/12.499944. 2
- [Neu05] J. Neumann, *Mikroskopische Untersuchungen zur laserinduzierten Blasenbildung und -dynamik an absorbierenden Mikropartikeln*, Inauguraldissertation, Universität Lübeck (2005). 2, 8, 23
- [Ott61] M. Otter, *Temperaturabhängigkeit der optischen konstanten massiver metalle*, Zeitschrift für Physik A **161**(5), p. 539 (1961), url/doi: 10.1007/BF01341551. 23, 26, 43, 45
- [Pit03] C. M. Pitsillides, E. K. Joe, X. Wei, R. R. Anderson and C. P. Lin, *Selective Cell Targeting with Light-Absorbing Microparticles and Nanoparticles*, Biophys. J. **84**(6), p. 4023 (2003), url/doi: <http://www.biophysj.org/cgi/content/abstract/84/6/4023>. 2
- [Ple04] A. Plech, V. Kotaidis, S. Gresillon, C. Dahmen and G. von Plessen, *Laser-induced heating and melting of gold nanoparticles studied by time-resolved x-ray scattering*, Phys. Rev. B **70**(19), p. 195423 (2004), url/doi: <http://link.aps.org/abstract/PRB/v70/e195423>. 9, 11, 47
- [Ple07] A. Plech, R. Cerna, V. Kotaidis, F. Hudert, A. Bartels and T. Dekorsy, *A surface phase transition of supported gold nanoparticles*, Nano Lett. **7**(4), p. 1026 (2007), url/doi: 10.1021/nl070187t. 7
- [Pus06] V. K. Pustovalov, *Investigation of threshold laser intensities for melting and evaporation of spherical and spheroidal nanoparticles in media by short laser pulses*, Chem. Phys. Lett. **421**, p. 142 (2006). 9
- [Sch90] P. Schiebener and J. Straub, *Refractive index of water and steam as function of wavelength, temperature and density*, J. Phys. Chem. Ref. Data **19**(3), p. 677 (1990). 23, 26
- [Wag00] Wagner, Haslbeck, S. L., C. S., P. Q. A. and M. K.-P., *Before striking gold in gold-ruby glass*, Nature **407**(12), p. 691 (2000). 1
- [Wil98] J. P. Wilcoxon, J. E. Martin, F. Parsapour, B. Wiedenman and D. F. Kelley, *Photoluminescence from nanosize gold clusters*, J. Chem. Phys. **108**(21), p. 9137 (1998), url/doi: 10.1063/1.476360. 9, 31
- [Wil02] O. M. Wilson, X. Hu, D. G. Cahill and P. V. Braun, *Colloidal metal particles as probes of nanoscale thermal transport in fluids*, Phys. Rev. B **66**(22), p. 224301 (2002), url/doi: 10.1103/PhysRevB.66.224301. 9, 47
- [Yav94] O. Yavas, P. Leiderer, H. K. Park, C. P. Grigoropoulos, C. C. Poon, W. P. Leung, N. Do and A. C. Tam, *Optical and acoustic study of nucleation*

Bibliography

- and growth of bubbles at a liquid-solid interface induced by nanosecond-pulsed-laser heating*, Appl. Phys. A **58**(4), p. 407 (1994), url/doi: 10.1007/BF00323618. 2
- [Yav97] O. Yavas, A. Schilling, J. Bischof, J. Boneberg and P. Leiderer, *Bubble nucleation and pressure generation during laser cleaning of surfaces*, Appl. Phys. A **64**(4), p. 331 (1997), url/doi: 10.1007/s003390050487. 2
- [Zap91] W. Zapka, W. Ziemlich and A. C. Tam, *Efficient pulsed laser removal of 0.2 μm sized particles from a solid surface*, Appl. Phys. Lett. **58**(20), p. 2217 (1991), url/doi: 10.1063/1.104931. 2
- [Zha05] V. P. Zharov, R. R. Letfullin and E. N. Galitovskaya, *Microbubbles-overlapping mode for laser killing of cancer cells with absorbing nanoparticle clusters*, J. Phys. D: Appl. Phys. **38**(15), p. 2571 (2005), url/doi: <http://stacks.iop.org/0022-3727/38/2571>. 2

Acknowledgements

Der englischsprachige Leser wird es mir verzeihen, dass ich die Danksagungen in meiner Muttersprache verfasse. Viele Menschen verdienen an dieser Stelle einen besonderen Dank:

- Prof. Dr. Johannes Boneberg, ohne dessen engagierte und fachkundige Betreuung mit zahllosen Diskussionen, fachspezifisch wie fachfremd, mir die Arbeit nur halb soviel Spaß bereitet hätte,
- Prof. Dr. Paul Leiderer, der sehr viel Wert auf eine angenehme Arbeitsatmosphäre an seinem Lehrstuhl legt und seine Mitarbeiter mit trickreichen Fragen immer wieder zu Höstleistungen anspornt,
- Prof. Dr. Thomas Dekorsy für die Übernahme des Zweitgutachtens,
- Dr. Anton Plech, ein wahrer Experte auf dem Gebiet der Plasmonen, ohne dessen Ratschläge meine Arbeit in dieser Form gar nicht möglich gewesen wäre,
- der gesamten “Diplozimmer”-Crew, besonders aber Andreas Kolloch und Stephen Riedel fürs Korrekturlesen,
- Louis Kukk, der mich jetzt hoffentlich doch nicht als Lehrling in seiner Feinmechanik-Werkstatt anstellen muss, für diverse Details und Anregungen rund um meinen Aufbau,
- den “Doktos”, die in Notfällen auch abends und am Wochenende unter “2627” erreichbar sind,
- Regina Bauer, dass sie für mich da ist wenn ich sie brauche,
- meinen Eltern, deren Unterstützung mir schon immer sehr viel bedeutet hat.